Controllability assessment and fault-tolerant sizing of UAVs under effector failures

F Pollet, Jonathan Liscouët, Marc Budinger, Scott Delbecq, Jean-Marc Moschetta

Controllability assessment and fault-tolerant sizing of UAVs under effector failures

F. Pollet *
ISAE-SUPAÉRO, Université de Toulouse, 10 Avenue Edouard Belin, 31400 Toulouse, France

J. Liscouët †
Concordia University, 1455 De Maisonneuve Blvd., Montreal, QC H3G 1M8, Canada

M. Budinger ‡
ICA, Université de Toulouse, UPS, INSA, ISAE-SUPAERO, MINES-ALBI, CNRS, 3 rue Caroline Aigle, 31400 Toulouse, France

S. Delbecq §
ISAE-SUPAÉRO, Université de Toulouse, 10 Avenue Edouard Belin, 31400 Toulouse, France

J.-M. Moschetta ¶
ISAE-SUPAÉRO, Université de Toulouse, 10 Avenue Edouard Belin, 31400 Toulouse, France

This article presents a methodology for analyzing the controllability and fault-tolerant sizing of fixed-wing and hybrid fixed-wing vertical landing and takeoff (FW-VTOL) unmanned aerial vehicles (UAVs). Building upon previous research focused on multirotor UAVs, the study introduces a new control authority index, redefined dynamics models, and enhanced control allocation techniques to address rotor failures and lock-in-place failures of control surfaces. The methodology considers effector limitations and the unidirectional drag condition for control surface deflection angles. These advancements are combined to assess the linear controllability and accomplish fault-tolerant sizing of UAVs. By applying the proposed methodology to a case study, the linear controllability of fixed-wing and hybrid FW-VTOL UAVs is evaluated in various failure scenarios. The results demonstrate that the hybrid FW-VTOL concept exhibits higher fault tolerance capability due to the presence of VTOL rotors that can compensate for control surface failures. The study emphasizes the importance of oversizing VTOL rotors to ensure sufficient control authority in double failure scenarios, revising the conventional assumption that VTOL system sizing primarily relies on takeoff analysis. The proposed advancements are relevant to future UAV designs intended for fault-tolerant applications such as medical equipment transport and air taxis.

*Ph.D. Candidate, ISAE-SUPAÉRO, Department of Aerospace Vehicles Design and Control (DCAS); felix.pollet@isae-supaero.fr
†Associate Professor, Concordia University, High Reliability Aerospace Design Lab (HiRAD); jonathan.liscouet@concordia.ca (Corresponding Author)
‡Professor, ICA/INSA Toulouse, Mechanical Engineering Department
§Associate Professor, ISAE-SUPAÉRO, Department of Aerospace Vehicles Design and Control (DCAS)
¶Professor, ISAE-SUPAÉRO, Aerodynamics, Energetics and Propulsion Department (DAEP)

Nomenclature

$\mathbf{A}$	=	state matrix
$\mathbf{B}$	=	control matrix
$\mathbf{B_f}$	=	control effectiveness matrix
$\mathbf{H}$	=	failure matrix
$\mathbf{x}$	=	state vector
$\mathbf{u}$	=	virtual control vector
$\mathbf{f}$	=	rotor thrust vector
$\mathbf{K}$	=	sizing factors vector
m_a	=	UAV total mass, kg
I_x, I_y, I_z	=	UAV moments of inertia, kg.m^2
p, q, r	=	roll, pitch, yaw rotational speeds, rad/s
u_b, v_b, w_b	=	longitudinal, lateral, vertical speeds, m/s
X, Y, Z	=	longitudinal, lateral, vertical control forces, N
L, M, N	=	roll, pitch, yaw control moments, N.m
ϕ, θ, ψ	=	roll, pitch, yaw angles, rad
$\boldsymbol{\delta}$	=	control input vector
ρ, η, ζ	=	aileron, elevator, rudder deflection angles, rad
τ	=	propeller thrust setting

Superscripts

$'$	=	failure case

Subscripts

$_0$	=	reference flight conditions

I. Introduction

For the past two decades, unmanned aerial vehicles (UAVs), also known as drones, have been intensively developed to cover a broad spectrum of applications, including: transport, agriculture, emergency response, aerial inspection, and urbanism, among others [1–5]. To meet these diversifying needs, designers have developed different concepts such as multirotor, fixed-wing and hybrid fixed-wing vertical takeoff and landing (FW-VTOL) configurations. Many prospective applications of UAV technologies are safety-critical, including flying ambulances, medical equipment transport, and air taxis in urban environments and beyond visual lines of sight. Technical failure as the result of an uncontrollable UAV could be catastrophic if the vehicle collides with humans, aircraft, helicopters, or infrastructures. Therefore, the design

of such vehicles must be driven by safety considerations in addition to the classical energy efficiency considerations. Here, safety refers to the ability of a faulty system to maintain control objectives, as the safety of a UAV largely depends on this control in the event of failure. Hence, the emergence of UAVs for safety-critical applications will depend on the ability to investigate and compare various design concepts and optimize their sizing for different mission and safety specifications.

Accordingly, our objective is to develop a new methodology combining a controllability assessment and fault-tolerant sizing of UAVs to evaluate and explore various designs for safety-critical applications. The article's scope involves the design of a fixed-wing and hybrid FW-VTOL UAV with fixed rotor thrust directions. The proposed methodology provides a framework for further adaptations to other types of propulsion, such as vectoring control or articulated rotor systems.

In previous research, the authors believe they captured a gap in sizing methodologies for high-reliability multicopters [6, 7]. To cover this gap, a new conceptual design methodology was introduced [8]. This methodology includes a systematic reliability calculation and sizing based on failure cases. For this purpose, linear controllability and reliability analysis methods are linked to an analytical sizing methodology. The controllability analysis and the sizing methodology are interconnected through the introduction of failure case sizing factors. The sizing process is based on a modern analytical approach that does not require a database and incorporates multidisciplinary design optimization, enabling design customization and computational efficiency. However, this methodology is limited to multirotor designs.

The multirotor design methodology introduced in reference [8] needs to be adapted and advanced to other concepts, such as concepts of fixed-wing and hybrid FW-VTOL. Specifically, the sizing methodology and controllability analysis must be further advanced. The focus of this article is the development of new linear controllability analysis and fault-tolerant sizing.

Based on the controllability matrix rank check, the classical controllability theory is limited to linear time-invariant systems with unconstrained inputs. It does not consider specific characteristics of drone designs, such as unidirectional rotors and nonlinear dynamics. Several alternative approaches have been developed to address these limitations and assess the controllability of multirotor and fixed-wing aircraft. Du et al. [9] introduced a method that evaluates the attainable control set to assess the controllability of linearized multicopter models around hover, considering input constraints and vehicle weight. Hassan [10] developed a method based on the Lie algebraic rank condition for assessing the controllability of nonlinear fixed-wing aircraft, but without considering constrained inputs. Other methods such as null controllability [11, 12], empirical gramian [13], and local strong accessibility [14, 15] offer interesting alternatives for evaluating the controllability of constrained-input nonlinear systems like multirotor UAVs. However, these methods have not been adapted and applied to fixed-wing aircraft or hybrid FW-VTOL UAVs. Building upon previous work [8], this paper extends a linear approach to address the specific challenges posed by constrained inputs and efforts symmetric around a neutral position governed by even functions, such as control surface drag, within the context of

hybrid FW-VTOL UAVs. Although the presented study does not delve into the alternative nonlinear approaches, it is worth exploring their application and adaptation to hybrid FW-VTOL designs in future research.

Fault-tolerant sizing cannot be achieved without control allocation for failure cases. Previous work of the authors [8] introduced sizing factors to cover the power demand of the propulsion system for failure cases. Yet, the methodology relied on a pseudo-inverse control allocation approach, which does not allow for systematic handling of constraints on the flight controls [16]. In addition, it does not accommodate nonlinearities, such as control surface drag, making it unsuitable for extending to control surface sizing. Alternative control allocation methods based on optimization overcome these limitations [16, 17]. However, these methods do not provide any degree of freedom in the effectors sizing to reach the effort demand, as discussed in Section V. Hence, the state-of-the-art lacks a consistent controllability analysis and fault-tolerant sizing for fixed-wing and FW-VTOL designs.

The present work introduces a new control authority index and an approach for defining UAV dynamics models and control allocation by addressing rotor and control surface nonlinearities and different failure conditions. These novelties are combined into a methodology for controllability assessment and fault-tolerant sizing. More specifically, a linearized UAV model is derived and modified for failure cases. Lock-in-place failures are introduced into the state-space model and reflected in the controllability matrix. A new control authority index called the extended available control authority index (XACAI) is proposed to evaluate the linear controllability of the UAV around trimmed states. This index considers nonlinear factors like control surface drag and applies to loss-of-effectiveness and lock-in-place failures. The UAV's trimmed state is calculated with a new control allocation problem formulation addressing effector limitations and failure cases. The resulting state-space model enables the verification of the controllability matrix rank to complete the local controllability assessment. The control analysis and effector sizing are interconnected by introducing sizing factors in the control allocation problem formulation. The effectiveness of the proposed linear controllability analysis and fault-tolerant sizing methodology is validated and demonstrated with a case study evaluating and comparing two equivalent fixed-wing and hybrid FW-VTOL UAVs.

This article is organized as follows: the scope of the controllability assessment is discussed in Section II. A linear flight dynamics model and its adaptation to critical failure cases are introduced in Section III. A new control authority index, the XACAI, is presented in Section **??**. The control re-allocation problem for failure cases is presented in Section V. The overall methodology for control analysis is described in Section VI and applied to two equivalent fixed-wing and hybrid FW-VTOL UAVs in Section VII. Section VIII concludes the article.

II. Scope of the controllability assessment

This section aims to discuss the controllability analysis of multirotor, fixed-wing and FW-VTOL UAVs and highlight the theoretical gap addressed by the introduction of the extended available control authority index (XACAI) in Section **??**.

For safety-critical systems, fault tolerance is defined as the possibility of achieving control objectives in the presence of faults [18]. Various strategies, including adaptive control, reliable control, and reconfigurable control, can achieve fault tolerance with or without explicit fault diagnosis [19]. The success of these strategies presupposes the existence of a solution to the control problem. In this sense, the possibility of finding a controller that satisfies the control objectives for the faulty UAV is a property of the system, which is called *reconfigurability* [20]. Inadequate reconfigurability, for example, insufficient redundancy, prevents effective fault tolerance, regardless of the control strategy [21]. Reconfigurability can be evaluated through controllability and observability analyses. The present research focuses on the controllability analysis of UAVs in the presence of one or multiple effector failures. Observability, and thereby sensor failures, are outside the scope of this study.

The proposed approach, described in Section VI, involves conducting a linear controllability analysis by examining a linear model of the drone in its trimmed states. It is important to note that the non-controllability of the linear model does not necessarily imply non-controllability in a nonlinear sense or in practical scenarios. An illustration of this concept can be seen in the geometric control strategy, which allows the accomplishment of linearly uncontrollable maneuvers by breaking them down into locally controllable segments [10, 22]. Other applications enable sacrificing yaw control to achieve specific maneuvers such as emergency landing [23–26]. In the specific case under study, it is crucial for the control scheme to bring the speeding vehicle to a complete stop and transition to a hover mode before initiating a controlled descent in the event of a failure occurring during a cruise flight. This procedure necessitates sufficient control over all virtual control axes, including heave and attitude controls [6]. Therefore, in this study, controllability analysis is based on the principle that the UAV must have the capability to maintain complete or reduced control over all virtual control axes, thus preventing any potential catastrophic failures. Consequently, it is essential for the drone to exhibit linear controllability in the vicinity of the trimmed state after a failure.

The classical controllability theory, which relies on the controllability matrix rank check, deals with linear time-invariant systems. While it assesses the inherent controllability of linear models and serves as a necessary condition for linear controllability, it is inadequate for multirotor and fixed-wing designs. This is due to its inability to account for the limitations imposed by the bounded and unidirectional nature of rotors [27]. To overcome this limitation, Du et al. [9] expanded upon the positive controllability theory applied to linear autonomous systems introduced by Brammer [28]. They introduced the concept of ACAI [9], which quantifies the available control capabilities by measuring the remaining attainable control set, considering factors such as constrained rotor thrusts and vehicle weight. The controllability of the linear model is assessed by combining the controllability rank check and the ACAI, which serve as necessary and sufficient conditions [9]. This way, the ACAI provides an effective approach to address the controllability challenges associated with multirotor designs subject to constrained control efforts. However, fixed-wing and FW-VTOL designs involve additional nonlinearities in control efforts during operation and under specific failure conditions, such as control surface jamming and control surface drag, as outlined in Section III and **??** respectively. When a control

surface jamming occurs, it can be considered as the introduction of a new disturbance while fixing the associated control variable. Furthermore, The surface drag results in symmetric efforts around a neutral position governed by even functions, leading to a nonlinear control effectiveness matrix incompatible with ACAI computation. Therefore, a new approach is required to address these challenges. In this study, the XACAI is introduced to extend the ACAI calculations to a nonlinear control effectiveness matrix and is combined with control allocation optimization to address the introduction of disturbances caused by failures. The XACAI calculations are detailed in Section **??**, while the controllability conditions and their applicability are summarized in Table 1.

Table 1 Controllability conditions of linear time-invariant models and their applicability.

Assumptions on control inputs	**Necessary and sufficient conditions for linear controllability**	**Examples of applications**
Unconstrained linear control inputs	Controllability matrix is full rank	• Multirotor UAVs with pitch-controlled propellers
Bounded unidirectional control inputs	Controllability matrix is full rank and ACAI is stricly positive	• Multirotor UAVs with fixed propellers • Multirotor UAVs with pitch-controlled propellers
Bounded unidirectional control inputs and efforts governed by even functions (nonlinear control effectiveness matrix)	Controllability matrix is full rank and XACAI is strictly positive	• Fixed-wing and FW-VTOL UAVs • Multirotor UAVs with fixed propellers • Multirotor UAVs with pitch-controlled propellers

III. UAV dynamics model

This section introduces the UAV dynamics state space model linearized and reformulated to represent rotor and control surface loss of effectiveness and lock-in-place failures. The dynamics model is illutrated with a FW-VTOL UAV concept.

A. Non-linear state-space model

The UAV model is obtained following a standard approach based on Newton's second law of motion. The rotation speed vector $\mathbf{\Omega} = [p \quad q \quad r]^T$ and the translation speed vector $\mathbf{V} = [u_b \quad v_b \quad w_b]^T$ are expressed in the UAV body frame of reference. Deriving the dynamic equations in an inertial frame of reference provides the following dynamic model:

$$\begin{cases} m_a(\dot{\mathbf{V}} + \mathbf{\Omega} \times \mathbf{V}) = \mathbf{F} \\ \mathbf{I}.\dot{\mathbf{\Omega}} + \mathbf{\Omega} \times \mathbf{I}.\mathbf{\Omega} = \mathbf{M} \end{cases} \tag{1}$$

where m_a denotes the mass of the UAV and $\mathbf{I}$ denotes the inertia matrix. The external forces $\mathbf{F}$ [N] and external moments $\mathbf{M}$ [N.m] are due to the propulsive, aerodynamic and gravitational efforts acting on the UAV. The external efforts are either control or perturbation efforts. The propulsion system and the control surfaces generate the control efforts. The perturbation efforts come from the gravity effect and the aerodynamics of fixed surfaces (e.g., fuselage drag). The

external forces and moments are divided accordingly:

$$\begin{bmatrix} \mathbf{F} \\ \mathbf{M} \end{bmatrix} = \begin{bmatrix} \mathbf{F_u} \\ \mathbf{M_u} \end{bmatrix} + \begin{bmatrix} \mathbf{F_{pert}} \\ \mathbf{M_{pert}} \end{bmatrix}, \tag{2}$$

where subscripts $_{\cdot \mathbf{u}}$ and $_{\cdot \mathbf{pert}}$ refer to the control efforts and perturbation efforts, respectively. The force and moment components of the control efforts are denoted as X, Y, Z and L, M, N, respectively, and are represented by the virtual control vector $\mathbf{u} \in \mathbb{R}^6$:

$$\mathbf{u} = [X \quad Y \quad Z \quad L \quad M \quad N]^T \tag{3}$$

The virtual control vector components are functions of the control effector states and control effectiveness matrix $\mathbf{B_f} \in \mathbb{R}^{6\times m}$, with m being the number of effectors, as follows:

$$\mathbf{u} = \mathbf{B_f}\boldsymbol{\delta}, \tag{4}$$

The control effectiveness matrix, which reflects the configuration and geometry of the UAV design, is further developed in Section **??**. The control input vector $\boldsymbol{\delta} \in \mathbb{R}^m$ in Equation 4 contains the effectors' inputs such as the propeller thrust settings $\tau \in [0, 1]$ and the deflection angles [rad] of the elevators (η), ailerons (ρ), and rudders (ζ) [29]:

$$\boldsymbol{\delta} = [\rho_1, \cdots, \rho_i, \eta_1, \cdots, \eta_j, \zeta_1, \cdots, \zeta_k, \tau_1, \cdots, \tau_l]^T \tag{5}$$

The detailed scalar equations of motions, derived from the above equalities, can be found in VIII. The motion variables and control notations introduced above are visually summarized in Figure 1, where $\boldsymbol{\Phi} = [\phi \quad \theta \quad \psi]^T$ represents the Euler angles (i.e., roll, pitch and yaw).

B. Linearized state-space model

The equations of motion are linearized using the small-disturbance theory applied to a reference flight condition. For example, the longitudinal speed becomes $u_b = u_{b_0} + \Delta u_b$, where Δ represents a deviation from the referenced value. For simplicity, the flight condition of reference consists of a steady, straight and level flight, which implies:

$$v_{b_0} = w_{b_0} = p_0 = q_0 = r_0 = \phi_0 = \psi_0 = 0. \tag{6}$$

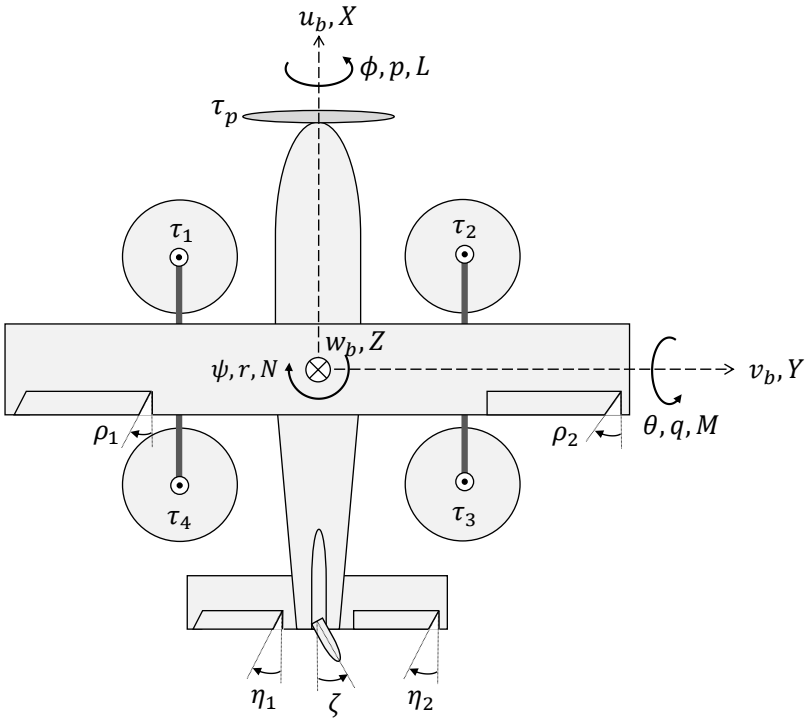

Fig. 1 Motion variables and control notations of a FW-VTOL UAV concept.

The equations of motion are reduced to a linear form by applying a first-order approximation, which yields the following flight dynamics model:

$$\Delta\dot{\mathbf{x}} = \mathbf{A}\Delta\mathbf{x} + \mathbf{B}\Delta\mathbf{u} \tag{7}$$

$$\mathbf{A} = f(\mathbf{V_0}, \boldsymbol{\Omega_0}, \boldsymbol{\Phi}_0, \boldsymbol{\delta}_0) \tag{8}$$

$$\mathbf{B} = \begin{bmatrix} \mathbf{J_f}^{-1} \\ \mathbf{0}_{3\times 6} \end{bmatrix}, \mathbf{J_f} = \text{diag}\left(m_a, m_a, m_a, I_x, I_y, I_z\right) \tag{9}$$

where $\Delta\mathbf{x} = [\Delta u_b \quad \Delta v_b \quad \Delta w_b \quad \Delta p \quad \Delta q \quad \Delta r \quad \Delta\phi \quad \Delta\theta \quad \Delta\psi]^T \in \mathbb{R}^9$ is the state vector, $\mathbf{A} \in \mathbb{R}^{9\times 9}$ is the state matrix, and $\mathbf{B} \in \mathbb{R}^{9\times 6}$ is the control matrix.

The state matrix reflects the UAV's configuration and aerodynamics around the reference flight conditions. For a

perfectly trimmed fixed-wing UAV in symmetrical level flight, $\mathbf{A}$ is given by [29]:

$$\mathbf{A} = \begin{bmatrix} \dot{X}_u & 0 & \dot{X}_w & 0 & 0 & 0 & 0 & -g\cos\theta_0 & 0 \\ 0 & \dot{Y}_v & 0 & \dot{Y}_p & 0 & \dot{Y}_r - u_{b_0} & g\cos\theta_0 & 0 & 0 \\ \dot{Z}_u & 0 & \dot{Z}_w & 0 & \dot{Z}_q + u_{b_0} & 0 & 0 & -g\sin\theta_0 & 0 \\ 0 & \dot{L}_v & 0 & \dot{L}_p & 0 & \dot{L}_r & 0 & 0 & 0 \\ \dot{M}_u & 0 & \dot{M}_w & 0 & \dot{M}_q & 0 & 0 & -g\dot{M}_w\sin\theta_0 & 0 \\ 0 & \dot{N}_v & 0 & \dot{N}_p & 0 & \dot{N}_r & 0 & 0 & 0 \\ 0 & 0 & 0 & 1 & 0 & 0 & 0 & 0 & 0 \\ 0 & 0 & 0 & 0 & 1 & 0 & 0 & 0 & 0 \\ 0 & 0 & 0 & 0 & 0 & 1 & 0 & 0 & 0 \end{bmatrix} \tag{10}$$

The parameters $\dot{X}$, $\dot{Y}$, $\dot{Z}$, $\dot{L}$, $\dot{M}$ and $\dot{N}$ are aerodynamic stability derivatives [30]. Their expressions can be found in [29]. The detailed set of linearized scalar equations can be found in VIII.

The deviation of the virtual control vector in Equation 7, $\Delta\mathbf{u}$, is further developed to include the contributions of the effectors:

$$\Delta\mathbf{u} = \mathbf{u} - \mathbf{u_0} = \mathbf{B_f}\boldsymbol{\delta} - \mathbf{u_0}, \tag{11}$$

where $\mathbf{u_0}$ is obtained from the reference equilibrium condition and is representative of the perturbation efforts to be compensated. Finally, the state-space model is re-arranged as follows:

$$\Delta\dot{\mathbf{x}} = \mathbf{A}\Delta\mathbf{x} + \mathbf{B}\underbrace{(\mathbf{B_f}\boldsymbol{\delta} - \mathbf{u_0})}_{\Delta\mathbf{u}} \tag{12}$$

C. Failure cases

This subsection introduces a new flight dynamics model to address failure cases. The considered effectors (control surfaces and propellers) have two distinct failure modes: loss of effectiveness and lock-in-place. Both cases are discussed below.

Loss of effectiveness

A loss of effectiveness is characterized by a reduction of the effectiveness of one or more effectors with respect to a

nominal value. Practically, one or more effectors achieve a fraction of or no control command (i.e., complete failure). This failure mode is modeled by introducing a failure matrix, as described in [8, 9]:

$$\mathbf{H} = \text{diag}\left(\eta_1, \cdots, \eta_m\right), \tag{13}$$

where the parameter $\eta_i \in [0, 1]$ accounts for the loss of effectiveness of the i-th effector. A complete failure is characterized by $\eta_i = 0$. The control effectiveness matrix from Equation 4 becomes:

$$\mathbf{B_f'} = \mathbf{B_f H}, \tag{14}$$

with superscript $'$ representing the failure case.

Lock-in-place

Following an actuator's failure, for example, through a run-away or jamming, a control surface may be stuck in a fixed position that is usually different from zero. When a lock-in-place failure occurs, the control authority over the jammed surface is lost. Additionally, unwanted aerodynamic efforts, which have to be balanced by the remaining effectors, are introduced. This leads to a revision of the state-space model.

The state-space model is linearized about the same initial conditions (e.g., steady level flight) but with different reference inputs representing the new trimmed state. As for the loss of effectiveness, the contributions of the failed surfaces in the virtual control vector are set to zero (apply $\eta_i = 0$ for each jammed surface in Equation 13 to define $\mathbf{H}$). In addition, the efforts of the jammed surfaces are shifted to the perturbation efforts. In other words, the efforts of the jammed effectors are now part of the effort demand that must be satisfied by the remaining controls. This translates to:

$$\mathbf{u'} = \mathbf{B_f'}\boldsymbol{\delta} \tag{15}$$

$$\mathbf{u_0'} = \mathbf{u_0} - \mathbf{B_f}(\mathbf{I_m} - \mathbf{H})\boldsymbol{\delta}_0', \tag{16}$$

where $\mathbf{I_m} \in \mathbb{R}^m$ is the identity matrix. The second term in Equation 16 represents the additional efforts to be compensated. The vector $\boldsymbol{\delta}_0'$ contains the control inputs derived from the reference equilibrium condition, which are revised to reflect the modified trimmed state. Its full determination, the control allocation, is covered in Section V. Finally, the state matrix is updated to reflect the new reference condition:

$$\mathbf{A'} = f(\mathbf{V_0}, \boldsymbol{\Omega_0}, \boldsymbol{\Phi}_0, \boldsymbol{\delta}_0') = \mathbf{A} + \mathbf{A}_{\delta_0'}, \tag{17}$$

where $\mathbf{A}_{\delta_0'}$ represents the couplings introduced by the non-zero angles of the control surfaces in the trimmed state. For a

steady, straight, and level reference flight, $\mathbf{A}_{\delta'_0}$ is expressed as follows:

$$\mathbf{A}_{\delta'_0} = \frac{2}{u_{b_0}} \begin{bmatrix} \mathbf{B}\mathbf{B}_\mathbf{f}\boldsymbol{\delta}'_\mathbf{0} & \mathbf{0}_{9\times 8} \end{bmatrix} \tag{18}$$

The demonstration of Equation (18) is provided in VIII.

IV. Controllability assessment

This section synthesizes the calculation of the ACAI before proposing a new index encompassing VTOL, FW, and hybrid FW-VTOL designs.

A. Available Control Authority Index (ACAI)

The ACAI computation introduced by Du et al. [9] is based on a linear state-space model of multirotor drones in hovering conditions, such as:

$$\dot{\mathbf{x}} = \mathbf{A}\mathbf{x} + \mathbf{B}(\mathbf{u} - \mathbf{u_0}) \tag{19}$$

where $\mathbf{x}$ is the state vector, $\mathbf{A}$ is the state matrix, $\mathbf{B}$ represents the control matrix, $\mathbf{u} = [Z \quad L \quad M \quad N]^T \in \mathbb{R}^4$ represents the virtual control vector, and $\mathbf{u_0}$ represents the control vector derived at the reference state $\mathbf{x_0}$.
The main component of the control authority is the previously defined virtual control vector $\mathbf{u}$, which results from the rotor thrust vector $\mathbf{f}$ as follows [9]:

$$\mathbf{u} = \mathbf{B}_\mathbf{f}\mathbf{f} \tag{20}$$

where $\mathbf{B}_\mathbf{f} \in \mathbb{R}^{4\times m}$ is the control effectiveness matrix, $\mathbf{f} \in \mathbb{R}^m$ is the rotor thrust vector, and m is the number of rotors. Each rotor provides a purely positive and limited thrust, leading to the following constraint set for the rotor thrust vector [9]:

$$\mathcal{F} = \left\{ \mathbf{f} \middle| \mathbf{f} = [f_1, \cdots, f_m]^T,\ 0 \le f_i \le f_{max,i} \right\} \tag{21}$$

where f_i is the thrust of i-th rotor and $f_{max,i}$ is the maximum thrust [N] of the i-th rotor. Equations (21) and (22) provide the virtual control vector constraint set [9]:

$$\Omega = \{\mathbf{u} | \mathbf{u} = \mathbf{B}_\mathbf{f}\mathbf{f}, \mathbf{f} \in \mathcal{F}\} \tag{22}$$

The ACAI quantifies the maximum effort achievable in all control directions (specifically, Z, L, M, and N), taking into account the impact of constrained rotor thrusts and the influence of a disturbance, such as the weight of the vehicle. More specifically, if $\mathbf{u_0}$ is contained within Ω, then the ACAI is the radius of the largest enclosed four-dimensional sphere centered at $\mathbf{u_0}$ in Ω. If $\mathbf{u_0}$ is not contained within Ω, then the ACAI is the radius of the largest enclosed sphere centered at $\mathbf{u_0}$ in the complementary set of Ω, denoted as Ω^c [9]:

$$\rho\left(\mathbf{u_0}, \partial\Omega\right) \triangleq \begin{cases} \min\{||\mathbf{u_0} - \mathbf{u}|| : \mathbf{u_0} \in \Omega, \mathbf{u} \in \partial\Omega\} \\ -\min\{||\mathbf{u_0} - \mathbf{u}|| : \mathbf{u_0} \in \Omega^c, \mathbf{u} \in \partial\Omega\} \end{cases} \tag{23}$$

where $\partial\Omega$ is the boundary of Ω.

As demonstrated in [31], $\partial\Omega$ is a polytope of parallel hyper-plane segments. In an n-dimensional space, these hyper-plane segments have a dimension of $n-1$. The ACAI is based on calculating the minimum distance between each parallel hyper-plane segment and projecting $\mathbf{u_0}$ on the axis of each of these minimum distances. Evaluating whether each projection of $\mathbf{u_0}$ lies between the hyper-plane segments or not determines if $\mathbf{u_0}$ is contained within Ω. We define the hyper-plane segment matrices $\mathbf{B_{f1,k}} \in \mathbb{R}^{n\times(n-1)}$ with n as the dimension of the virtual control vector (here, $n = 4$) by isolating the column vectors of the set of $n-1$ effectors defining the k-th hyper-plane segments in $\mathbf{B_f}$. In addition, $\mathbf{B_{f2,k}} \in \mathbb{R}^{n\times(m-n+1)}$ represents the complementary matrix of $\mathbf{B_{f1,k}}$. It comprises the column vectors of $\mathbf{B_f}$, which are excluded from $\mathbf{B_{f1,k}}$. Accordingly, $\mathbf{f}$ and $\mathbf{B_f}$ are partitioned as follows:

$$\mathbf{u} = \mathbf{B_f f} = \begin{bmatrix} \mathbf{B_{f1,k}} & \mathbf{B_{f2,k}} \end{bmatrix} \begin{bmatrix} \mathbf{f_{1,k}} \\ \mathbf{f_{2,k}} \end{bmatrix} = \mathbf{B_{f1,k}} \mathbf{f_{1,k}} + \mathbf{B_{f2,k}} \mathbf{f_{2,k}}, \tag{24}$$

where $\mathbf{f_{1,k}} \in \mathbb{R}^{n-1}$ and $\mathbf{f_{2,k}} \in \mathbb{R}^{m-n+1}$ are the corresponding partitions of $\mathbf{f}$. $k = [1, \cdots, p]$ indexes the sets of hyper-plane segments of $\delta\Omega$, where p is the number of combinations of $n-1$ effectors out of m. The axis of the minimum distance between the k-th parallel hyper-plane segments is defined by a unit vector, $\boldsymbol{\xi}_k \in \mathbb{R}^n$, orthogonal to these segments. By definition, $\boldsymbol{\xi}_k$ belongs to the null space of the column space of $\mathbf{B_{f1}, k}$. Hence, $\boldsymbol{\xi}_k$ satisfies [9]:

$$\mathbf{B_{f1,k}}^T \boldsymbol{\xi}_k = 0 \text{ and } ||\boldsymbol{\xi}_k|| = 1 \tag{25}$$

The following ACAI calculation, initially introduced by Du et al. [9], is modified for bidirectional effectors and simplicity. The hyperplane-segment center is expressed as:

$$\mathbf{F_c} = \mathbf{B_f} \begin{bmatrix} c_1 & \cdots & c_m \end{bmatrix}^T \tag{26}$$

With c_i being the center of the i-th control variable's range:

$$c_i = \frac{f_{max,i} + f_{min,i}}{2} \tag{27}$$

where $f_{max,i}$ and $f_{min,i}$ are the maximum and minimum thrust [N] of the i-th rotor, respectively. The distance between the k-th hyper-plane segments and their center of symmetry $\mathbf{F_c}$ is obtained by fixing the values of $\mathbf{f_{2,k}}$ at their extrema and allowing the remaining $n-1$ elements of $\mathbf{f_{1,k}}$ to vary between their limits [31]. This distance is obtained as [9]:

$$d = \frac{1}{2} \left| {\boldsymbol{\xi}_k}^T \mathbf{B_{f2,k}} \right| |\mathbf{\Delta}_k| \tag{28}$$

The vector of the effector magnitudes is defined as:

$$\mathbf{\Delta}_k = [\alpha_{k_1} \quad \cdots \quad \alpha_{k_p}] \tag{29}$$

where α_{k_i} represents the magnitude of the i-th effector of the k-th hyperplane-segment set: $\alpha_{k_i} = f_{max,k_i} - f_{min,k_i}$. To evaluate whether $\mathbf{u_0}$ resides between or outside the hyperplane segments, we compare distances as follows:

$$d_k = \underbrace{\frac{1}{2} \left| {\boldsymbol{\xi}_k}^T \mathbf{B_{f2}, k} \right| |\mathbf{\Delta}_k|}_{\substack{\text{distance between } k\text{-th} \\ \text{hyperplane-segment and } \mathbf{F_c}}} - \underbrace{\left| {\boldsymbol{\xi_k}}^T \left(\mathbf{F_c} - \mathbf{u_0} \right) \right|}_{\substack{\text{distance between} \\ \mathbf{u_0} \text{ and } \mathbf{F_c}}} \tag{30}$$

According to Equation (23), the ACAI is given by:

$$\rho(\mathbf{u_0}, \partial\Omega) = \min\left(d_1, \cdots, d_p\right) \tag{31}$$

Finally, as demonstrated by Du et al. [9], a configuration is locally controllable in all directions of $\mathbf{u}$ (i.e., Z, L, M, and N) only if

$$C(\mathbf{A}, \mathbf{B}) \text{ has full rank and } \rho\left(\mathbf{u_0}, \partial\Omega\right) > 0 \tag{32}$$

where $C(\mathbf{A}, \mathbf{B})$ is the system's controllability matrix.

B. Hybrid FW-VTOL UAV Control Effectiveness Model

In the case of hybrid FW-VTOL UAVs, we assume level flight under steady conditions. This implies negligible angles of attack, bank angle, side-slip angle, and a constant air velocity along the flight direction. Control along the y-axis of the UAV is primarily achieved through fixed surfaces such as the wing and horizontal stabilizer. Moreover,

there exists a coupling between the y-axis and the other axes, enabling control of the UAV's vertical motion by acting on these other axes. Therefore, we consider a four-dimensional virtual control vector, denoted as $\mathbf{u} = [X \quad L \quad M \quad N]^T$. The effector control vector, represented as $\boldsymbol{\delta} = \begin{bmatrix}\rho_1 & \rho_2 & \eta_1 & \eta_2 & \zeta & \tau_p & \tau_1 & \tau_2 & \tau_3 & \tau_4\end{bmatrix}^T$, corresponds to the configuration illustrated in Figure 1. For consistency with the notations introduced in Section 2, the effector control vector $\boldsymbol{\delta}$ replaces the rotor thrust vector notation $\mathbf{f}$ used in the ACAI computation presented in Section IV.A.

Drag forces are essential aerodynamic components that introduce cross-coupling effects between control axes in the control surfaces. The drag forces must therefore be included in the assessment of control authority, specifically in the calculation of the control effectiveness matrix. These forces exhibit symmetric behavior governed by even functions, which can be approximated as absolute functions. As a result, the control effectiveness equations become highly nonlinear:

$$\begin{aligned}
X &= \dot{X}_{\rho_1}|\rho_1| + \dot{X}_{\rho_2}|\rho_2| + \dot{X}_{\eta_1}|\eta_1| + \dot{X}_{\eta_2}|\eta_2| + \dot{X}_{\zeta}|\zeta| + \dot{X}_{\tau_p}\tau_p \\
L &= \dot{L}_{\rho_1}\rho_1 + \dot{L}_{\rho_2}\rho_2 + \dot{L}_{\eta_1}\eta_1 + \dot{L}_{\eta_2}\eta_2 + \dot{L}_{\zeta}\zeta + \dot{L}_{\tau_p}\tau_p + \dot{L}_{\tau_1}\tau_1 + \dot{L}_{\tau_2}\tau_2 + \dot{L}_{\tau_3}\tau_3 + \dot{L}_{\tau_4}\tau_4 \\
M &= \dot{M}_{\rho_1}\rho_1 + \dot{M}_{\rho_2}\rho_2 + \dot{M}_{\eta_1}\eta_1 + \dot{M}_{\eta_2}\eta_2 + \dot{M}_{\zeta}|\zeta| + \dot{M}_{\tau_1}\tau_1 + \dot{M}_{\tau_2}\tau_2 + \dot{M}_{\tau_3}\tau_3 + \dot{M}_{\tau_4}\tau_4 \\
N &= \dot{N}_{\rho_1}|\rho_1| + \dot{N}_{\rho_2}|\rho_2| + \dot{N}_{\eta_1}|\eta_1| + \dot{N}_{\eta_2}|\eta_2| + \dot{N}_{\zeta}\zeta + \dot{N}_{\tau_1}\tau_1 + \dot{N}_{\tau_2}\tau_2 + \dot{N}_{\tau_3}\tau_3 + \dot{N}_{\tau_4}\tau_4
\end{aligned} \tag{33}$$

where $\dot{X}_i, \dot{L}_i, \dot{M}_i, \dot{N}_i$ [N] are the control derivatives of the i-th effector on each axis. The control derivatives for the i-th propeller result from its maximum thrust f_{max} and positions x_{τ_i}, y_{τ_i} along the x-axis and y-axis, respectively:

$$\dot{L}_{\tau_i} = C_T \rho_{air} n_{max}^2 D^4 y_{\tau_i} = f_{max} y_{\tau_i} \tag{34}$$

$$\dot{M}_{\tau_i} = C_T \rho_{air} n_{max}^2 D^4 x_{\tau_i} = f_{max} x_{\tau_i} \tag{35}$$

$$\dot{N}_{\tau_i} = \omega_{\tau_i} C_Q \rho_{air} n_{max}^2 D^5 \tag{36}$$

where ρ_{air} [kg/m^3] is the air density, n_{max} is the propeller speed for maximum thrust, D is the propeller diameter, and C_T [-] and C_Q [-] are the thrust and torque coefficients, respectively. The sense of rotation of the propeller is represented by ω_{τ_p}, which is equal to 1 for a clockwise rotation and -1 for a counterclockwise rotation. The control derivatives of the control surfaces reflect the aerodynamic effects due to their deflections. For example, on the x-axis:

$$\dot{X}_i = \frac{1}{2} \rho_{air} v_{air}^2 S_i C_{x,i} \tag{37}$$

where v_{air} [m/s] is the relative air velocity, S_i [m^2] the i-th control surface area, and $C_{x,i}$ [-] is the aerodynamic coefficient specific to the i-th control surface geometry, profile, kinematics, and x-axis.

The presence of non-linearities, particularly the absolute functions in Equation (33), prevents the calculation of ACAI as presented in Section IV.A. To address this limitation, the following section introduces a new index to handle

these non-linearities.

C. Extended Available Control Authority Index (XACAI)

The proposed XACAI extends the computation of ACAI to accommodate nonlinear control effectiveness matrices, including the one resulting from Equation (33).

Step 1: Calculate the unit vectors $\boldsymbol{\xi}_{fw,k}$.

To begin, the nonlinear control effectiveness matrix is linearized to calculate the unit vectors, $\boldsymbol{\xi}_{fw,k}$, which are orthogonal to the hyper-plane segments forming the boundary of the attainable control set:

$$\mathbf{B_{fw,lin}} = \begin{bmatrix} \dot{X}_{\rho_1} & \dot{X}_{\rho_2} & \dot{X}_{\eta_1} & \dot{X}_{\eta_2} & \dot{X}_{\zeta} & \dot{X}_{\tau_p} & 0 & 0 & 0 & 0 \\ \dot{L}_{\rho_1} & \dot{L}_{\rho_2} & \dot{L}_{\eta_1} & \dot{L}_{\eta_2} & \dot{L}_{\zeta} & \dot{L}_{\tau_p} & \dot{L}_{\tau_1} & \dot{L}_{\tau_2} & \dot{L}_{\tau_3} & \dot{L}_{\tau_4} \\ \dot{M}_{\rho_1} & \dot{M}_{\rho_2} & \dot{M}_{\eta_1} & \dot{M}_{\eta_2} & \dot{M}_{\zeta} & 0 & \dot{M}_{\tau_1} & \dot{M}_{\tau_2} & \dot{M}_{\tau_3} & \dot{M}_{\tau_4} \\ \dot{N}_{\rho_1} & \dot{N}_{\rho_2} & \dot{N}_{\eta_1} & \dot{N}_{\eta_2} & \dot{N}_{\zeta} & 0 & \dot{N}_{\tau_1} & \dot{N}_{\tau_2} & \dot{N}_{\tau_3} & \dot{N}_{\tau_4} \end{bmatrix} \tag{38}$$

We define each hyper-plane segment matrix, $\mathbf{B_{fw1,lin,k}} \in \mathbb{R}^{n\times(n-1)}$, by isolating the column vectors of the effectors of the k-th hyper-plane segments in $\mathbf{B_{fw,lin}}$, and $\boldsymbol{\xi}_{fw,k}$ is obtained by applying $\mathbf{B_{fw1,lin,k}}$ to Equation (25):

$$\mathbf{B_{fw1,lin,k}}^T \boldsymbol{\xi}_{fw,k} = 0 \text{ and } ||\boldsymbol{\xi}_{fw,k}|| = 1 \tag{39}$$

Step 2: Partition the control effectiveness matrix between linear and absolute control inputs.

ACAI calculation based on a linearized control effectiveness matrix such as Equation (38) would incorrectly assume that the drag forces can become propulsive and lead to an incorrect controllability assessment. Therefore, the nonlinear control effectiveness matrix $\mathbf{B_{fw}}$ is divided into linear matrices relative to linear and nonlinear control input vectors:

$$\mathbf{u} = \begin{bmatrix} \mathbf{B_{fw,l}} & \mathbf{B_{fw,nl}} \end{bmatrix} \begin{bmatrix} \boldsymbol{\delta} \\ |\boldsymbol{\delta}| \end{bmatrix} = \mathbf{B_{fw,l}}\boldsymbol{\delta} + \mathbf{B_{fw,nl}}|\boldsymbol{\delta}| \tag{40}$$

With $\mathbf{B_{fw,l}}$, the linear-term matrix, expressed as follows:

$$\mathbf{B_{fw,l}} = \begin{bmatrix} 0 & 0 & 0 & 0 & 0 & \dot{X}_{\tau_p} & 0 & 0 & 0 & 0 \\ \dot{L}_{\rho_1} & \dot{L}_{\rho_2} & \dot{L}_{\eta_1} & \dot{L}_{\eta_2} & \dot{L}_{\zeta} & \dot{L}_{\tau_p} & \dot{L}_{\tau_1} & \dot{L}_{\tau_2} & \dot{L}_{\tau_3} & \dot{L}_{\tau_4} \\ \dot{M}_{\rho_1} & \dot{M}_{\rho_2} & \dot{M}_{\eta_1} & \dot{M}_{\eta_2} & 0 & 0 & \dot{M}_{\tau_1} & \dot{M}_{\tau_2} & \dot{M}_{\tau_3} & \dot{M}_{\tau_4} \\ 0 & 0 & 0 & 0 & \dot{N}_{\zeta} & 0 & \dot{N}_{\tau_1} & \dot{N}_{\tau_2} & \dot{N}_{\tau_3} & \dot{N}_{\tau_4} \end{bmatrix} \tag{41}$$

And $\mathbf{B_{fw,nl}}$ the nonlinear term matrix:

$$\mathbf{B_{fw,nl}} = \begin{bmatrix} \dot{X}_{\rho_1} & \dot{X}_{\rho_2} & \dot{X}_{\eta_1} & \dot{X}_{\eta_2} & \dot{X}_{\zeta} & 0 & 0 & 0 & 0 & 0 \\ 0 & 0 & 0 & 0 & 0 & 0 & 0 & 0 & 0 & 0 \\ 0 & 0 & 0 & 0 & \dot{M}_{\zeta} & 0 & 0 & 0 & 0 & 0 \\ \dot{N}_{\rho_1} & \dot{N}_{\rho_2} & \dot{N}_{\eta_1} & \dot{N}_{\eta_2} & 0 & 0 & 0 & 0 & 0 & 0 \end{bmatrix} \tag{42}$$

The subsequent partitions $\begin{bmatrix} \mathbf{B_{fw1,l,k}} & \mathbf{B_{fw2,l,k}} \end{bmatrix}$ and $\begin{bmatrix} \mathbf{B_{fw1,nl,k}} & \mathbf{B_{fw2,nl,k}} \end{bmatrix}$ are obtained by isolating the column vectors of the set of effectors of the k-th hyper-plane segments in $\mathbf{B_{fw,l}}$ and $\mathbf{B_{fw,nl}}$ respectively.

Step 3: Compute the distances d_k from the linear and absolute terms.

$\mathbf{\Delta}_k$, the effector magnitude vector applied to $\mathbf{B_{fw2,l,k}}$, is provided by Equation (29). The effector magnitude vector of $\mathbf{B_{fw2,nl,k}}$, $\mathbf{\Delta}_{k,nl}$, is obtained by applying the absolute function to δ_i to determine $f_{min,i}$ and $f_{max,i}$ in Equation (27) before applying Equation (29). The minimum distance between the hyper-plane segment and $\mathbf{u_0}$ is then expressed as follows:

$$\begin{aligned} d_{fw,k} = \frac{1}{2} \Big(& \left| \boldsymbol{\xi}_{fw,k}{}^T \mathbf{B_{fw2,l,k}} \right| |\mathbf{\Delta}_k| + \left| \boldsymbol{\xi}_{fw,k}{}^T \mathbf{B_{fw2,nl,k}} \right| \left| \mathbf{\Delta}_{k,nl} \right| \Big) \\ & - \left| \boldsymbol{\xi}_{fw,k}{}^T \left(\mathbf{F_c} - \mathbf{u_0} \right) \right| \end{aligned} \tag{43}$$

Finally, equations (31) and (32) are applied to assess the controllability of the UAV.

The controllability in failure conditions is assessed by applying the failure matrix $\mathbf{H}$ to the control effectiveness matrices defined above, and replacing $\mathbf{u_0}$ by $\mathbf{u_0'}$ as per Equation (16). In addition, the rank check of the controllability matrix is verified with the updated state matrix $\mathbf{A'}$ from Equation (17).

V. Effector sizing for failure cases

Failure case sizing aims to size the control effectors such that the UAV will have sufficient control authority following any failure assessed as controllable. This sizing is achieved with sizing factors, as per previous work [8]. Therefore, this

section introduces the control allocation problem and a method to derive sizing factors associated with the failure cases.

A. Control allocation problem formulation

Consider the system defined in Equation 12. Control allocation aims to determine a control input vector $\boldsymbol{\delta}$ to achieve a desired virtual control effort $\mathbf{u}$:

$$\mathbf{B_f}\boldsymbol{\delta} = \mathbf{u} \tag{44}$$

For redundant systems, Equation 44 is generally underdetermined, and an infinite number of vectors $\boldsymbol{\delta}$ can be the solution, assuming the control allocation is feasible. A common way to deal with the non-uniqueness of solutions is to introduce a secondary objective, namely to minimize the energy cost of control allocation:

$$\begin{aligned} \min_{\boldsymbol{\delta}} \quad & J = ||\boldsymbol{\delta}|| \\ \text{s.t.} \quad & \mathbf{B_f}\boldsymbol{\delta} = \mathbf{u}, \end{aligned} \tag{45}$$

where $||.||$ is the l^2-norm. This formulation admits an explicit solution given by the Moore-Penrose pseudo-inverse [16]:

$$\boldsymbol{\delta} = \mathbf{B_f^+}\mathbf{u}, \text{ with } \mathbf{B_f^+} = \mathbf{B_f}^T(\mathbf{B_f}\mathbf{B_f}^T)^{-1} \tag{46}$$

However, the above solution does not account for constraints on the effectors' inputs. Consequently, the solution might be physically unfeasible. In addition, the pseudo-inverse method does not handle non-linearities in the control effectivenesses, as introduced in Section IV.B.

Among the alternative allocation methods, the optimization-based approaches allow for more complex problems to be solved, including constraints and non-linearities [16]. We propose to address the control allocation problem using the mixed optimization formulation, which consists of combining the allocation objective and energy objective as follows [17]:

$$\begin{aligned} \min_{\boldsymbol{\delta}} \quad & J = ||\mathbf{B_f}\boldsymbol{\delta} - \mathbf{u}||^2 + \lambda||\boldsymbol{\delta}||^2 \\ \text{s.t.} \quad & \boldsymbol{\delta_{min}} \leq \boldsymbol{\delta} \leq \boldsymbol{\delta_{max}}, \end{aligned} \tag{47}$$

where $\lambda \in [0, +\infty]$ represents the priority of the allocation objective ($\lambda = 0$) over the energy objective ($\lambda = +\infty$) and is usually chosen close to zero.

Finally, the problem formulation is combined with Equation 39 to include the non-linearities in the effectors' controls:

$$\begin{aligned} \min_{\boldsymbol{\delta}} \quad & J = ||\mathbf{B_{f,l}}\boldsymbol{\delta} + \mathbf{B_{f,nl}}|\boldsymbol{\delta}| - \mathbf{u}||^2 + \lambda||\boldsymbol{\delta}||^2 \\ \text{s.t.} \quad & \boldsymbol{\delta_{min}} \leq \boldsymbol{\delta} \leq \boldsymbol{\delta_{max}}, \end{aligned} \tag{48}$$

B. Proposed sizing control allocation

The control allocation problem introduced above aims at finding the optimal control inputs to achieve a virtual effort at the UAV level, given a pre-defined design of the control effectors. However, there is no guarantee that an exact solution to the allocation objective ($\mathbf{B_f}\boldsymbol{\delta} = \mathbf{u}$) exists. Indeed, the set of attainable virtual efforts $\mathbf{u}$ is limited by the effectors' design, reflected by the control effectiveness matrix and the saturation constraints. In particular, the unfeasibility of control allocation in the presence of effector failures is a direct consequence of poorly sized controls. To address this issue, we propose a new formulation of the problem described in 47 that enables a fault-tolerant sizing of the effectors while solving the control allocation problem.

Consider a predetermined sizing of the control effectors obtained by considering normal operations only. The initial sizing, such as the rudder area and propeller diameter, is not within the scope of this paper and is typically derived from effort specifications (e.g., rudder hinge moment, propeller thrust) or empirical data. The proposed methodology introduces sizing factors, which are multiplier factors applied to the specifications of the effectors, to incorporate failure scenarios within a resizing process [8]. Specifically, for a given failure case, a sizing factor represents an increase in the effectiveness of an effector relative to its initial sizing:

$$\widetilde{\mathbf{B}_\mathbf{f}'} = \mathbf{B}_\mathbf{f}'\mathbf{K} = \mathbf{B_f}\mathbf{H}\mathbf{K} \tag{49}$$

$$\mathbf{K} = \mathrm{diag}(k_1, \cdots, k_m) \in [1, +\infty]^m \tag{50}$$

where $\mathbf{B_f}$ is the control effectiveness matrix obtained from initial sizing, $\widetilde{\mathbf{B}_\mathbf{f}'}$ is the revised control effectiveness matrix, $\mathbf{H}$ is the failure matrix representative of the failure case, k_i is the sizing factor applied to the i-th effector, and $\mathbf{K}$ is the sizing factor vector. The effectiveness of an effector is directly related to its sizing, as shown in Equation (37). For instance, doubling the surface area of an aileron leads to a doubling of its effectiveness ($k_i = 2$). Similarly, doubling the maximum thrust of a rotor results in a twofold increase in its effectiveness.

The sizing factors must ensure that the allocation objective is achievable and that the resized system preserves a certain level of control authority. The preservation of control authority can be expressed by the following inequality:

$$\rho(\mathbf{u}_\mathbf{0}', \partial\widetilde{\Omega'}) \geq \alpha\rho(\mathbf{u_0}, \partial\Omega), \tag{51}$$

where $\rho(\mathbf{u}_\mathbf{0}', \partial\widetilde{\Omega'})$ represents the control authority index, specifically the XACAI, of the fault-tolerant sizing in the presence of failures. The required control authority can be alleviated in cases of failure based on the probability of occurrence. In this context, the parameter $\alpha \in [0, 1]$ quantifies the acceptable reduction in control authority under failure compared to the initial sizing during normal operating conditions.

The sizing factor vector and the control authority requirement are added to the control allocation problem expressed by

Equation (47), which leads to the following formulation:

$$
\begin{aligned}
\min_{\boldsymbol{\delta},\mathbf{K}} \quad & J = \underbrace{||\mathbf{B_f H K}\boldsymbol{\delta} - \mathbf{u}||^2}_{\substack{\text{allocation}\\ \text{objective}}} + \lambda \underbrace{||\mathbf{K}\boldsymbol{\delta}||^2}_{\substack{\text{energy}\\ \text{objective}}} + \epsilon \underbrace{||\mathbf{K} - \mathbf{I_m}||^2}_{\substack{\text{sizing}\\ \text{objective}}} \\
\text{s.t.} \quad & \boldsymbol{\delta_{min}} \leq \boldsymbol{\delta} \leq \boldsymbol{\delta_{max}}, \\
& \mathbf{K} \in [1, +\infty]^m, \\
& \rho(\mathbf{u_0'}, \partial\widetilde{\Omega'}) \geq \alpha\rho(\mathbf{u_0}, \partial\Omega),
\end{aligned}
\tag{52}
$$

where the last term in the function J represents the sizing minimization objective to minimize deviations from the initial sizing ($\mathbf{K} = \mathbf{I_m}$). Additional constraints can be imposed on the sizing factor vector, for example, to disable resizing of a specific effector or to restrict its oversizing. The parameters λ and ϵ are chosen to prioritize either allocation, energy, or sizing objectives. In practice, $\lambda \ll \epsilon \ll 1$. Finally, the allocation objective is to maintain the equilibrium condition, that is $\mathbf{u} = \mathbf{u_0'}$.

The nonlinear least-square problem described above can be solved using various optimization methods. This study utilizes a trust region algorithm [32] implemented in the Python library SciPy [33]. To ensure the robustness of the results, a multi-start strategy was adopted.

Finally, resolving this problem for all failure cases provides not only the trimmed positions of the effectors but also the maximum sizing factors vector $\mathbf{K_{max}} \in [1, +\infty]^m$

$$
\mathbf{K_{max}} = \left[\max(k_{1,1}, \cdots, k_{1,p}), \cdots, \max(k_{m,1}, \cdots, k_{m,p})\right] \tag{53}
$$

$$
= \left[k_{1,max}, \cdots, k_{m,max}\right], \tag{54}
$$

where $k_{i,j}$ is the optimal sizing factor for effector $i \in [1, m]$ and failure case $j \in [1, p]$, obtained by solving Equation 52. $k_{i,max}$ is the maximum sizing factor for control effector i, considering all possible failures. Applying K_{max} to the initial effectors' sizing leads to a new design that is robust to failures.

VI. Controllability assessment and fault-tolerant sizing methodology

Figure 2 represents the overall methodology for a systematic local controllability assessment and fault-tolerant sizing of UAVs under effector failures, using the extended design structure matrix (XDSM) notation [34]. Generic processes are depicted as green boxes, while parallelograms represent data inputs and outputs. Data connections are represented by vertical lines for inputs and horizontal lines for outputs. Thin black arrows indicate process connections. Stacked boxes indicate multiple executions corresponding to each failure case. The diagram shows a six-step procedure: concept definition, sizing optimization, XACAI calculation, control allocation, model revision for failure cases, and

rank check of the controllability matrix. The paper's scope is limited to the XACAI calculation, control allocation, model revision, and rank check.

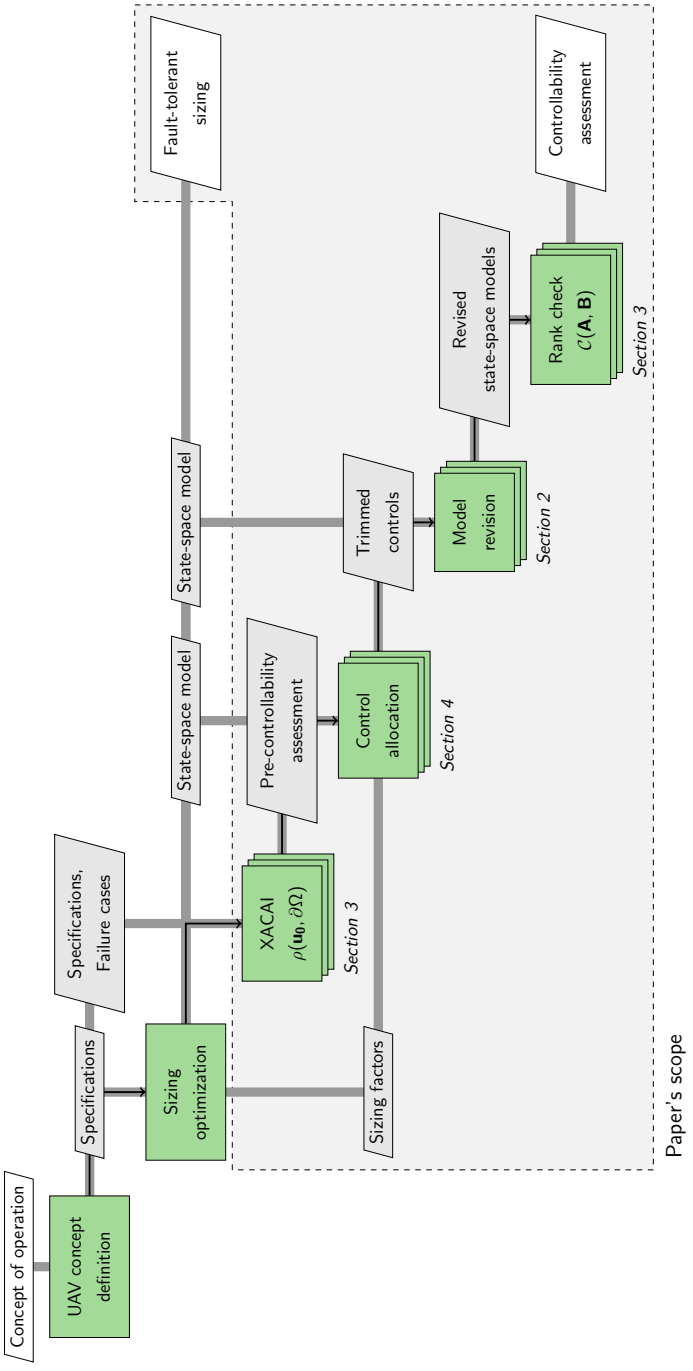

Fig. 2 Diagram of the proposed methodology using the extended design structure matrix (XDSM) notation [34].

The methodology starts by defining a concept of operation, which describes the characteristics of the unmanned aerial system from a user's perspective [35]. From the concept of operation, one or several candidate configurations of

UAVs are proposed, along with design specifications and failure case definitions. Specifications include performance requirements and technology assumptions to assist in the design process. Also included in the specifications is a parametric state-space model representative of the UAV configuration. From the specifications, the UAV is optimally sized. A methodology for the efficient sizing and optimization of multirotor drones is presented by the authors in [36, 37] and extended to fixed-wing and hybrid configurations in [38]. By effectively sizing the UAV, this process provides actual values representative of the design and flight conditions for the state-space model. In parallel, the controllability assessment for failure cases is initiated. The XACAI presented in Section IV.C is calculated for each failure case with non-restrictive effectiveness values for the effectors. This enables the identification of potentially controllable failure cases before the initiation of a fault-tolerant sizing. The actual sizing of the effectors is achieved via the sizing control allocation presented in Section V.B. The process takes the state-space model provided by the sizing optimization as inputs. The sizing factors required to ensure fault-tolerance are computed for each potentially controllable failure case. The resulting maximum sizing factors are then fed back into the sizing optimization so that the failure cases are included in the sizing process [8]. This procedure is repeated until convergence to an optimal, fault-tolerant sizing of the UAV. Once the sizing has converged, the state-space model of the UAV is revised for each failure case. This process requires knowledge of the trimmed controls derived from the control allocation. Finally, the full rank condition is verified on each linearized state-space model. Together with the previously calculated XACAI, this concludes the overall fault-tolerance assessment.

Supplemental material includes a Python script with functions implementing the controllability assessment and fault-tolerant sizing methodology.

VII. Case study

The case study detailed in this section illustrates the application of the methodology proposed in Section VI on two different concepts of UAVs and compares their fault-tolerance levels. Although the methodology may apply to any flight conditions by adjusting the linearized state-space model presented in Section III, for the purpose of simplicity and conciseness, this case study focuses on failures occurring in cruise flight conditions. The controllability analysis is separated into two parts. In the first part, only the loss of effectiveness failures are considered. Any single failure or combination of two failures is covered. The study does not extend to triple failures, as their probability of occurrence is too remote. Then, the lock-in-place failures of the control surfaces are evaluated to demonstrate the contribution of the methodology. Any single or double failure of the control surfaces is covered, and only the worst cases regarding aerodynamic efforts (i.e., full deflection of the control surfaces) are assessed. Additionally, this section covers any combination of a control surface lock-in-place failure with a propeller loss of effectiveness. Finally, the maximum sizing factors obtained from the worst cases are provided to ensure consistency between the effectors' sizing and controllability analysis.

A. Concepts definition

The first concept consists of a fixed-wing UAV with two ailerons, two elevators, one rudder and a single rotor located at the nose-tip, as illustrated in Figure 3. Its design reflects the E-flite Ultra Stick 25e [39], whose dynamics model, linearized around cruise flight conditions without failures, is provided in [40]. Expressly, this model assumes that the longitudinal and lateral dynamics are decoupled. The second concept consists of a hybrid FW-VTOL UAV with

Fig. 3 E-flite Ultra Stick 25e [39]

similar design specifications, except four VTOL rotors have been added. This concept is representative of the UAV depicted in Figure 1. On the y-axis, the VTOL rotors are centered on the right and left wings. On the x-axis, they are positioned on either side of the aerodynamic center, with a distance equal to twice the wing's mean aerodynamic chord. The thrust-to-weight ratios for the propulsion and the VTOL rotors are based on market trends. Furthermore, the total masses of both concepts are assumed to be equal. The additional mass introduced by the VTOL propulsion is assumed to be balanced by a lower battery capacity. The VTOL rotors are typically inactive in nominal cruise flight conditions. However, their activation in the event of a failure adds a layer of redundancy to the flight controls.

The specifications of both concepts are summarized in Table 2.

B. Controllability results

Loss of effectiveness

The results for loss of effectiveness failures are provided in Table 3. The controllability assessment indicates that the fixed-wing concept remains controllable after a complete loss of effectiveness of one aileron and/or one elevator. However, if both ailerons fail, the fixed-wing UAV is linearly uncontrollable. In fact, the XACAI is calculated as equal

Table 2 Specifications of the UAVs. Adapted from [40].

Parameter	Fixed-wing	Hybrid FW-VTOL
Mass	1.959 kg	1.959 kg
Wing span	1.27 m	1.27 m
Mean aerodynamic chord:	0.25 m	0.25 m
Moment of inertia I_x	0.089 kg.m^2	0.089 kg.m^2
Moment of inertia I_y	0.144 kg.m^2	0.144 kg.m^2
Moment of inertia I_z	0.162 kg.m^2	0.162 kg.m^2
Max. deflection angles	±25 deg	±25 deg
Thrust-to-weight ratio (forward propulsion)	0.35	0.35
Thrust-to-weight ratio (VTOL)	N/A	1.25

to zero, which reflects the absence of authority on the roll axis. In the absence of additional effectors for controlling the longitudinal axis, the fixed-wing UAV does not withstand the simultaneous failure of both elevators, as the controllability matrix is not full rank. Additionally, the fixed-wing concept is linearly uncontrollable if the rudder losses its effectiveness. The hybrid FW-VTOL remains controllable for any single or double failure thanks to its VTOL rotors.

Table 3 Results of the controllability assessment for loss of effectiveness failures.

Failures	Linear Controllability	
	Fixed-wing	Hybrid FW-VTOL
ρ_1 or ρ_2	Controllable	Controllable
η_1 or η_2	Controllable	Controllable
ζ	Uncontrollable	Controllable
$\rho_1\&\rho_2$	Uncontrollable	Controllable
$\eta_1\&\eta_2$	Uncontrollable	Controllable
$\rho_1\&\eta_1$ or $\rho_1\&\eta_2$ or $\rho_2\&\eta_1$ or $\rho_2\&\eta_2$	Controllable	Controllable
$\rho_1\&\tau_1$ or $\rho_1\&\tau_2$ or $\rho_1\&\tau_3$ or $\rho_1\&\tau_4$	N/A	Controllable
$\rho_2\&\tau_1$ or $\rho_2\&\tau_2$ or $\rho_2\&\tau_3$ or $\rho_2\&\tau_4$	N/A	Controllable

Note: "ρ_1 or ρ_2" represents the failure of either aileron 1 or aileron 2.
"$\rho_1\&\rho_2$" represents the failure of both aileron 1 and aileron 2.

Lock-in-place

The results for lock-in-place failures are provided in Table 4. The fixed-wing concept is not capable of withstanding any single lock-in-place failure, whereas the hybrid FW-VTOL concept maintains controllability in the presence of single or double lock-in-place failures, except for the rudder. To address a stuck rudder, the ailerons and VTOL rotors would need to be oversized by a factor greater than 3. However, this level of oversizing is impractical as it would significantly impact the UAV's initial design. Without considering triple failures, the controllability assessment clearly demonstrates the advantage of the hybrid FW-VTOL concept. Additionally, in the event of a jammed aileron or elevator, the activation of the VTOL rotors offers an advantageous control mechanism for maintaining balance in the roll and pitch axes. This

assumption relies on the prompt detection of the fault and the high responsiveness of the rotors.

Table 4 Results of the controllability assessment for lock-in-place failures.

Failures	Linear Controllability	
	Fixed-wing	Hybrid FW-VTOL
ρ_1 or ρ_2	Uncontrollable	Controllable
η_1 or η_2	Uncontrollable	Controllable
ζ	Uncontrollable	Uncontrollable[(1)]
$\rho_1\&\rho_2$	Uncontrollable	Controllable
$\eta_1\&\eta_2$	Uncontrollable	Controllable
$\rho_1\&\eta_1$ or $\rho_1\&\eta_2$ or $\rho_2\&\eta_1$ or $\rho_2\&\eta_2$	Uncontrollable	Controllable
$\rho_1\&\tau_1$ or $\rho_1\&\tau_2$ or $\rho_1\&\tau_3$ or $\rho_1\&\tau_4$	N/A	Controllable
$\rho_2\&\tau_1$ or $\rho_2\&\tau_2$ or $\rho_2\&\tau_3$ or $\rho_2\&\tau_4$	N/A	Controllable

[(1)] Controllability would require increasing the control effectiveness of the ailerons and VTOL rotors by a factor greater than 3.

C. Sizing factors

The controllability assessment has shown that the fixed-wing concept does not withstand any lock-in-place failure. This statement is valid regardless of the effectors' sizing. There exists no sizing factor that would result in a linearly controllable fixed-wing UAV. For the hybrid FW-VTOL concept, the sizing control allocation presented in Section V is applied to the failure scenarios assessed as controllable.

Several cases are analyzed, each corresponding to a distinct level of required control authority, as specified by Equation (51). The reference value for the XACAI is determined based on the initial sizing under normal operating conditions, without considering the involvement of the VTOL rotors. Subsequently, the sizing control allocation for failure cases includes the active VTOL rotors to ensure adequate control authority. The controllability results clearly demonstrated that relying solely on the control surfaces is insufficient to maintain controllability in the event of a lock-in-place failure. Table 5 presents a summary of the sizing control allocation cases, indicating the required control authority of the UAV in different failure cases relative to the reference XACAI value.

Table 5 Summary of the sizing control allocation cases and associated required control authorities after failure.

Case	Requirement on control authority	XACAI value
1	Control authority fully preserved	1.76
2	25% deterioration of control authority	1.32
3	50% deterioration of control authority	0.88
4	75% deterioration of control authority	0.44

Figure 4 presents the maximum sizing factors obtained when the UAV is subject to single and double lock-in-place failures. Table 6 provides an extract of the detailed results for three specific failure scenarios. It should be noted that,

given an aileron (or elevator) failure, an oversizing of the symmetrical aileron (or elevator) has been disabled to ensure design consistency. The results show that satisfaction of the allocation and control authority targets is achieved primarily by oversizing the VTOL rotors rather than the control surfaces. Low-speed flight conditions such as approach or landing generally drive the control surface sizing rather than the cruise flight scenario under study. Another reason for favouring the oversizing of the VTOL rotors is that controllability in failure scenarios is mainly made possible by the presence of VTOL rotors. The control authority is more sensitive to the sizing of the latter than that of any other effectors. In the most restrictive cases regarding control authority, oversizing of the rudder is essential.

The simultaneous jamming of both ailerons is the most critical failure for the VTOL rotors sizing, although the simultaneous failure of both elevators results in sizing factors that are only slightly lower. When the control authority must be fully preserved (case 1), the concurrent failure of an aileron and a VTOL rotor is critical for sizing the rudder. Similar results are found when a 25% alleviation of the required control authority is allowed (case 2).

The sizing factors for the VTOL rotors highlight the importance of considering double failure scenarios during high-speed conditions in the sizing process, revising the conventional assumption that the takeoff scenario is the main driver for sizing the VTOL propulsion system. To conduct a more comprehensive comparison of the maximum thrusts during cruise flight and takeoff, it is necessary to consider the variation in the thrust coefficient that occurs between these two flight phases [41].

The results indicate that in the case of single failures, no significant oversizing of the control surfaces and VTOL rotors is necessary. Only the most critical scenario for control authority, referred to as case 1, requires a minor oversizing of the rudder by 3%.

Table 6 Three examples of sizing control allocation results for fully preserved control authority (case 1).

Failure scenario 1 out of 67

	ρ_1	ρ_2	η_1	η_2	ζ	τ_p	τ_1	τ_2	τ_3	τ_4
Failures	×	×								
Control inputs $\boldsymbol{\delta}'_0$	25 deg	-25 deg	2.0 deg	2.0 deg	0.1 deg	0.31	0.83	0.01	0.03	0.69
Sizing factors	1.0	1.0	1.0	1.0	1.0	1.0	1.89	1.0	1.0	1.89

Failure scenario 2 out of 67

	ρ_1	ρ_2	η_1	η_2	ζ	τ_p	τ_1	τ_2	τ_3	τ_4
Failures			×	×						
Control inputs $\boldsymbol{\delta}'_0$	3.4 deg	6.6 deg	25 deg	25 deg	-1.1 deg	0.35	0.87	0.93	0.15	0.09
Sizing factors	1.0	1.0	1.0	1.0	1.0	1.0	1.77	1.77	1.0	1.0

Failure scenario 3 out of 67

	ρ_1	ρ_2	η_1	η_2	ζ	τ_p	τ_1	τ_2	τ_3	τ_4
Failures	×							×		
Control inputs $\boldsymbol{\delta}'_0$	-25 deg	-11.0 deg	-7.4 deg	-7.4 deg	3.8 deg	0.32	0.04	0	0.83	0.03
Sizing factors	1.0	1.0	1.0	1.0	1.27	1.0	1.0	1.0	1.05	1.0

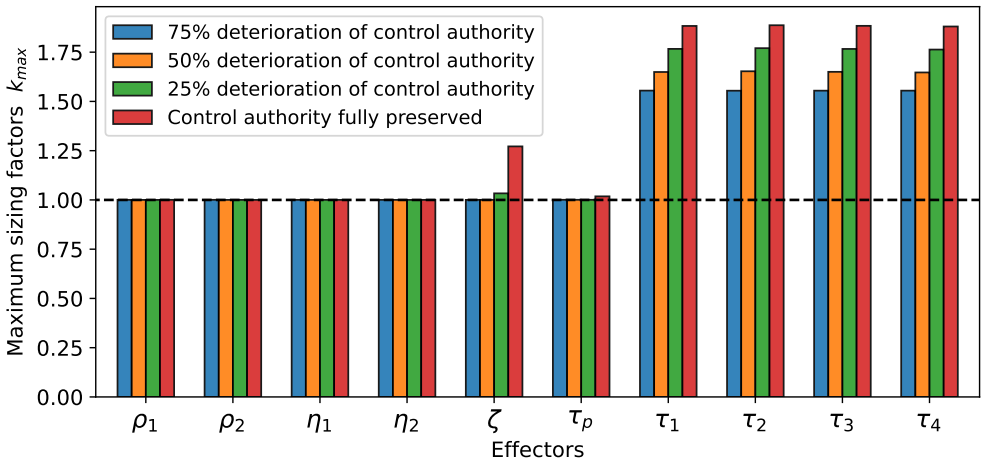

Fig. 4 Maximum sizing factors obtained for the hybrid FW-VTOL concept subject to single and double lock-in-place failures, for different control authority requirements.

Finally, a comparison between the XACAI and ACAI approaches highlights the methodological improvement. Figure 5 illustrates the maximum sizing factors for the most restrictive case of control authority, considering the inclusion (XACAI) and exclusion (ACAI) of control surface drag. The sizing of the VTOL rotors remains unchanged, as it is determined by the forces acting on the roll. However, the sizing of the rudder is influenced by the forces acting on the yaw, which include the rudder itself, drag forces from the deflection of other control surfaces, and to a lesser extent, the VTOL rotors. Therefore, accounting for the yaw moment generated by drag forces is crucial for accurately sizing the rudder. The ACAI approach, which neglects drag forces, fails to recognize the need for oversizing the rudder.

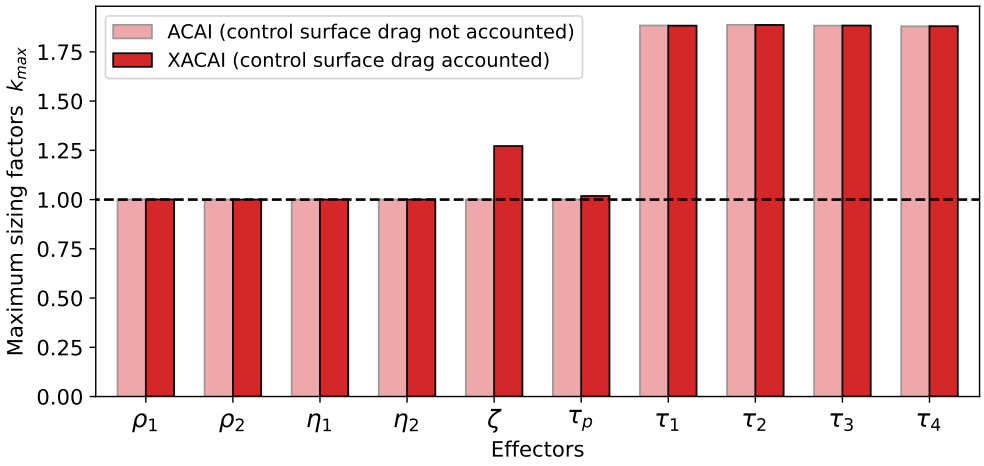

Fig. 5 Comparison of the maximum sizing factors for the hybrid FW-VTOL concept under single and double lock-in-place failures, considering fully preserved control authority (case 1), using the ACAI and XACAI approaches.

VIII. Conclusion

The present article introduces and combines a new control authority index and approach for defining UAV dynamics models and control allocations by addressing rotor and control-surface non-linearities and failure conditions. In doing so, it adapts and advances previously introduced controllability analyses and fault-tolerant sizing methods for multirotor UAVs [8] to other concepts such as fixed-wing and hybrid FW-VTOL concepts. The contributions of this methodology are twofold. First, it enables the linear controllability analysis of fixed-wing and hybrid FW-VTOL UAVs equipped with control surfaces and rotors. Second, it fills the gap between controllability, failure scenarios, and the sizing of effectors.

To this end, a linearized UAV model is derived and modified for failure cases. Specifically, lock-in-place failures (e.g., control surface jamming or run-away) are introduced into the state-space model and reflected in the controllability matrix. Another significant contribution of this article is the development of a new control authority index, the XACAI, which addresses non-linearities such as control surface drag and lock-in-place failures in the control efforts. The UAV is linearly controllable only if the XACAI is positive and the controllability matrix is full rank. Verifying the second condition requires calculating the UAV's trimmed state, which is obtained by solving a control allocation problem. The control analysis and the effectors' sizing are linked by introducing sizing factors in a new formulation of the control allocation problem.

The case study demonstrates the effectiveness of the proposed methodology, evaluating the linear controllability of a fixed-wing UAV and a hybrid FW-VTOL concept in various failure scenarios. The study focuses on a steady-level flight condition for simplicity and conciseness. The results highlight the higher fault tolerance of the hybrid FW-VTOL concept due to the presence of additional effectors (VTOL rotors) that can be utilized in case of failures. However, the study also reveals the need for oversizing the VTOL rotors to ensure sufficient control authority during double failure scenarios, revising the conventional assumption of basing VTOL system sizing solely on takeoff analysis. Furthermore, the comparison between the ACAI and XACAI approaches reveals that the ACAI method underestimates the necessary oversizing of the rudder by overlooking the impact of incorporating control surface drag into the sizing analysis. This discrepancy underscores the significance of the proposed XACAI approach.

Further research should address the following limitations of the presented work. The methodology proposed in this study supports the evaluation of the intrinsic reconfigurability of UAVs through a linear controllability analysis. The controllability assessment is applied to a linearized system model and offers a sufficient condition for preserving or restoring control authority on the virtual control axes. It is important to note that this controllability assessment does not exclude the possibility of nonlinear controllability in the system, as discussed in Section II. In addition, the methodology is time-independent and does not capture the dynamics of the effectors, which limits the accuracy of the assessment. Including or adding constraints to control response times could significantly increase this accuracy. The link between controllability and sizing could be further consolidated by integrating the proposed methodology into a multidisciplinary design framework and introducing new penalties on the sizing factors to reflect economic and

design limitations. With these improvements, the proposed methodology will provide a novel and effective means to explore and evaluate UAV design alternatives at the conceptual and preliminary development stages for safety-critical applications requiring fault tolerance.

Appendix

Equations of motion

Scalar equations of motion

$$X + q_d S C_{x_0} - m_a g \sin\theta = m_a(\dot{u_b} + q w_b - r v_b) \tag{55}$$

$$Y + q_d S C_{y_0} + m_a g \cos\theta \sin\phi = m_a(\dot{v_b} + r u_b - p w_b) \tag{56}$$

$$Z + q_d S C_{z_0} + m_a g \cos\theta \cos\phi = m_a(\dot{w_b} + p v_b - q u_b) \tag{57}$$

$$L + q_d S C_{l_0} = I_x \dot{p} - I_{xz}\dot{r} + qr(I_z - I_y) - I_{xz} pq \tag{58}$$

$$M + q_d S C_{m_0} = I_y \dot{q} + rp(I_x - I_z) + I_{xz}(p^2 - r^2) \tag{59}$$

$$N + q_d S C_{n_0} = -I_{xz}\dot{p} + I_z \dot{r} + pq(I_y - I_x) + I_{xz} qr \tag{60}$$

q_d is the dynamic pressure [Pa], S is the UAV reference area [m^2], C_{axis} are the aerodynamic coefficients of the fixed surfaces (e.g., wing and fuselage), and I are the moments of inertia [kg.m^2]. ϕ, θ and ψ are the roll [rad], pitch [rad], and yaw [rad] angles. X, Y, Z, L, M, and N are the control efforts [N] originating from the propellers and the control surfaces.

Linearized equations of motion in steady, straight, and level flight The linearized set of equations is obtained using the small-disturbance notation and neglecting the products of deviations (first order approximation), according to [29].

$$\frac{\Delta X}{m_a} + \dot{X}_u \Delta u_b + \dot{X}_w \Delta w_b - g\cos\theta_0 \Delta\theta = \Delta\dot{u_b} \tag{61}$$

$$\frac{\Delta Y}{m_a} + \dot{Y}_v \Delta v_b + \dot{Y}_p \Delta p + (\dot{Y}_r - u_{b_0})\Delta r + g\cos\theta_0 \Delta\phi = \Delta\dot{v_b} \tag{62}$$

$$\frac{\Delta Z}{m_a} + \dot{Z}_u \Delta u_b + \dot{Z}_w \Delta w_b + (\dot{Z}_q + u_{b_0})\Delta q - g\sin\theta_0 \Delta\theta = \dot{w_b} \tag{63}$$

$$\frac{\Delta L}{I_x} + \dot{L_v} \Delta v_b + \dot{L_p} \Delta p + \dot{L_r} \Delta r = I_x \dot{p} \tag{64}$$

$$\frac{\Delta M}{I_y} + \dot{M}_u \Delta u_b + \dot{M}_w \Delta w_b + \dot{M}_q \Delta q - g\dot{M}_w \sin\theta_0 = I_y \dot{q} \tag{65}$$

$$\frac{\Delta N}{I_z} + \dot{N}_v \Delta v_b + \dot{N}_p \Delta p + \dot{N}_r \Delta r = I_z \dot{r}, \tag{66}$$

where the parameters $\dot{X}$, $\dot{Y}$, $\dot{Z}$, $\dot{L}$, $\dot{M}$, $\dot{N}$ are aerodynamic stability coefficients obtained by a Taylor series expansion

applied to the efforts' variation about the reference equilibrium condition [29]. For instance,

$$\dot{X_u} \approx \frac{\rho_{air} v_{air}^2 S C_{D_0}}{m_a u_{b_0}}, \tag{67}$$

where C_{D_0} [-] is the parasitic drag coefficient of the airframe, ρ_{air} [kg.m^{-3}] is the air density, and S [m^2] is the reference area.

The insignificant aerodynamic derivatives in Equations 61 have been neglected.

State-space model for failure cases

For better understanding, the modification of the state-space model for failures cases is demonstrated in a first place on the x-axis, and focusing on an elevator. The scalar equation of motion on the x-axis, provided in VIII, is re-written with a focus on the effort originating from the elevator, for clarity:

$$X_\eta + X_{others} = m_a(\dot{u_b} + q w_b - r v_b), \tag{68}$$

where X_{others} are the efforts originating from the fixed surfaces, gravity, and control effectors, excluding the failed elevator. The effort from the elevator, X_η, is expressed as follows:

$$X_\eta = \frac{1}{2}\rho_{air} v_{air}^2 S_\eta C_{x,\eta} \eta \tag{69}$$

With S_η [m^2] the elevator's area and $C_{x,\eta}$ [-] its aerodynamic coefficient specific to the x-axis, assumed to be constant. The above equation is linearized around straight and level flight conditions, that is $u_b = u_{b_0} + \Delta u_b$, $v_b = \Delta v_b$ and $w_b = \Delta w_b$. The air velocity is expressed from a first order approximation as:

$$v_{air} = \sqrt{u_b^2 + v_b^2 + w_b^2} \tag{70}$$

$$= \sqrt{u_{b_0}^2 + 2u_{b_0}\Delta u_b + \Delta u_b^2 + \Delta v_b^2 + \Delta w_b^2} \tag{71}$$

$$\approx \sqrt{u_{b_0}^2 + 2u_{b_0}\Delta u_b}, \tag{72}$$

The elevator's effort on the x-axis becomes:

$$X_\eta = \frac{1}{2}\rho_{air}(u_{b_0}^2 + 2u_{b_0}\Delta u_b) S_\eta C_{x,\eta}(\eta_0 + \Delta\eta) \tag{73}$$

$$= \frac{1}{2}\rho_{air} u_{b_0}^2 S_\eta C_{x,\eta}\Delta\eta + \frac{1}{2}\rho_{air} u_{b_0}^2 S_\eta C_{x,\eta}\eta_0 + \rho_{air} u_{b_0} S_\eta C_{x,\eta}\eta_0 \Delta u_b \tag{74}$$

Introducing the elevator's control derivative, $\dot{X_\eta} = \frac{1}{2}\rho_{air} u_{b_0}^2 S_\eta C_{x,\eta}$, one obtains:

$$X_\eta = \dot{X_\eta}\Delta\eta + \dot{X_\eta}\eta_0 + \frac{2}{u_{b_0}}\dot{X_\eta}\eta_0\Delta u_b \tag{75}$$

$$= \dot{X_\eta}\eta + \frac{2}{u_{b_0}}\dot{X_\eta}\eta_0\Delta u_b \tag{76}$$

Generalizing to all effectors' controls and efforts yields the following virtual control vector:

$$\mathbf{u} = \mathbf{B_f}\boldsymbol{\delta} + \frac{2}{u_{b_0}}\mathbf{B_f}\boldsymbol{\delta_0}\Delta u_b \tag{77}$$

The state-space model becomes

$$\Delta\dot{\mathbf{x}} = \mathbf{A}\Delta\mathbf{x} + \mathbf{B}\left(\mathbf{B_f}\boldsymbol{\delta} + \frac{2}{u_{b_0}}\mathbf{B_f}\boldsymbol{\delta_0}\Delta u_b - \mathbf{u_0}\right) \tag{78}$$

$$= \left(\mathbf{A} + \frac{2}{u_{b_0}}\begin{bmatrix}\mathbf{B}\mathbf{B_f}\boldsymbol{\delta_0} & \mathbf{0}_{9\times 8}\end{bmatrix}\right)\Delta\mathbf{x} + \mathbf{B}(\mathbf{B_f}\boldsymbol{\delta} - \mathbf{u_0}) \tag{79}$$

Finally, taking into account the failures yields:

$$\Delta\dot{\mathbf{x}} = (\underbrace{\mathbf{A} + \frac{2}{u_{b_0}}\begin{bmatrix}\mathbf{B}\mathbf{B_f}\boldsymbol{\delta_0'} & \mathbf{0}_{9\times 8}\end{bmatrix}}_{\mathbf{A}_{\delta_0'}})\Delta\mathbf{x} + \mathbf{B}[\underbrace{\mathbf{B_f}\mathbf{H}}_{\mathbf{B_f'}}\boldsymbol{\delta} - \underbrace{(\mathbf{u_0} - \mathbf{B_f}(\mathbf{I_m} - \mathbf{H})\boldsymbol{\delta_0'})}_{\mathbf{u_0'}}] \tag{80}$$

Study case

State-space matrices of the Hybrid FW-VTOL concept.

The full-order state matrix, control matrix and control effectiveness matrix for the hybrid FW-VTOL UAV described in the case study (Section VII) are provided below. The system is linearized around cruise flight conditions, without failures, with a longitudinal speed $u_{b_0} = 19m/s$ [40].

$$\mathbf{A_0} = \begin{bmatrix} -0.38 & 0 & 0.60 & 0 & 0 & 0 & 0 & -9.80 & 0 \\ 0 & -0.64 & 0 & 0.46 & 0 & -18.21 & 9.50 & 0 & 0 \\ -0.98 & 0 & -10.65 & 0 & 16.74 & 0 & 0 & -0.21 & 0 \\ 0 & -2.02 & 0 & -12.47 & 0 & 4.05 & 0 & 0 & 0 \\ 0.18 & 0 & -5.39 & 0 & -16.55 & 0 & 0 & 0 & 0 \\ 0 & 1.30 & 0 & 0.86 & 0 & -3.09 & 0 & 0 & 0 \\ 0 & 0 & 0 & 1 & 0 & 0 & 0 & 0 & 0 \\ 0 & 0 & 0 & 0 & 1 & 0 & 0 & 0 & 0 \\ 0 & 0 & 0 & 0 & 0 & 1 & 0 & 0 & 0 \end{bmatrix} \tag{81}$$

$$\mathbf{B} = \begin{bmatrix} \mathbf{J_f}^{-1} \\ \mathbf{0}_{3\times 6} \end{bmatrix}, \quad \mathbf{J_f} = \mathrm{diag}(1.959, 1.959, 1.959, 0.089, 0.144, 0.162) \tag{82}$$

$$\mathbf{B_f} = \begin{bmatrix} 0. & 0. & -0.35 & -0.35 & 0. & 6.73 & 0. & 0. & 0. & 0. \\ 0. & 0. & 0. & 0. & 5.84 & 0. & 0. & 0. & 0. & 0. \\ 0. & 0. & -3.55 & -3.55 & 0. & 0. & 6.01 & 6.01 & 6.01 & 6.01 \\ -6.19 & 6.19 & 0. & 0. & 0.58 & 0.02 & 1.91 & -1.91 & -1.91 & 1.91 \\ 0. & 0. & -10.19 & -10.19 & 0. & 0. & 3.00 & 3.00 & -3.00 & -3.00 \\ 1.39 & -1.39 & 0. & 0. & -4.28 & 0. & 0.03 & -0.03 & 0.03 & -0.03 \end{bmatrix} \tag{83}$$

Funding Sources

The authors disclosed receipt of the following financial support for the research, authorship, and/or publication of this article: This work was supported by Mitacs through the Mitacs Globalink Program [grant number IT27116]; Natural Sciences & Engineering Research Council through the Discovery Program [grant number RGPIN-2022-05166]; The French National Research Agency (ANR) through the "Programme d'Investissements d'Avenir" [ANR-17-EURE-0005]; and ISAE-SUPAERO Foundation through the International Exchange Program.

References

[1] Lamptey, E., and Serwaa, D., "The Use of Zipline Drones Technology for COVID-19 Samples Transportation in Ghana," *HighTech and Innovation Journal*, Vol. 1, No. 2, 2020, pp. 67–71. https://doi.org/10.28991/HIJ-2020-01-02-03, URL https://hightechjournal.org/index.php/HIJ/article/view/18, number: 2.

[2] Vu, N. A., Dang, D. K., and Le Dinh, T., "Electric propulsion system sizing methodology for an agriculture multicopter," *Aerospace Science and Technology*, Vol. 90, 2019, pp. 314–326. https://doi.org/10.1016/j.ast.2019.04.044, URL https://www.sciencedirect.com/science/article/pii/S1270963818306424.

[3] Scott, J. E., and Scott, C. H., "Drone Delivery Models for Medical Emergencies," *Delivering Superior Health and Wellness Management with IoT and Analytics*, edited by N. Wickramasinghe and F. Bodendorf, Healthcare Delivery in the Information Age, Springer International Publishing, 2020, pp. 69–85. https://doi.org/10.1007/978-3-030-17347-0_3, URL https://doi.org/10.1007/978-3-030-17347-0_3.

[4] Shafiee, M., Zhou, Z., Mei, L., Dinmohammadi, F., Karama, J., and Flynn, D., "Unmanned Aerial Drones for Inspection of Offshore Wind Turbines: A Mission-Critical Failure Analysis," *Robotics*, Vol. 10, No. 1, 2021, p. 26. https://doi.org/10.3390/robotics10010026, URL https://www.mdpi.com/2218-6581/10/1/26, number: 1 Publisher: Multidisciplinary Digital Publishing Institute.

[5] Videras Rodríguez, M., Melgar, S. G., Cordero, A. S., and Márquez, J. M. A., "A Critical Review of Unmanned Aerial Vehicles (UAVs) Use in Architecture and Urbanism: Scientometric and Bibliometric Analysis," *Applied Sciences*, Vol. 11, No. 21, 2021, p. 9966. https://doi.org/10.3390/app11219966, URL https://www.mdpi.com/2076-3417/11/21/9966, number: 21 Publisher: Multidisciplinary Digital Publishing Institute.

[6] Nazarudeen, S. B., and Liscouët, J., "State-Of-The-Art And Directions For The Conceptual Design Of Safety-Critical Unmanned And Autonomous Aerial Vehicles," *2021 IEEE International Conference on Autonomous Systems (ICAS)*, IEEE, 2021, pp. 1–5. https://doi.org/10.1109/ICAS49788.2021.9551158.

[7] Warren, R., and Liscouët, J., "Comparative Analysis of Sizing Methodologies for High-Reliability Multicopters," *AIAA AVIATION 2022 Forum*, American Institute of Aeronautics and Astronautics, 2022, p. 3883. https://doi.org/10.2514/6.2022-3883, URL http://arc.aiaa.org/doi/10.2514/6.2022-3883.

[8] Liscouet, J., Pollet, F., Jézégou, J., Budinger, M., Delbecq, S., and Moschetta, J.-M., "A methodology to integrate reliability into the conceptual design of safety-critical multirotor unmanned aerial vehicles," *Aerospace Science and Technology*, 2022, p. 107681. https://doi.org/10.1016/j.ast.2022.107681.

[9] Du, G.-X., Quan, Q., Yang, B., and Cai, K.-Y., "Controllability Analysis for Multirotor Helicopter Rotor Degradation and Failure," *Journal of Guidance, Control, and Dynamics*, Vol. 38, No. 5, 2015, pp. 978–985. https://doi.org/10.2514/1.G000731, URL https://arc.aiaa.org/doi/10.2514/1.G000731.

[10] Hassan, A. M., and Taha, H. E., "Geometric control formulation and nonlinear controllability of airplane flight dynamics," *Nonlinear Dynamics*, Vol. 88, No. 4, 2017, pp. 2651–2669. https://doi.org/10.1007/s11071-017-3401-9, URL https://doi.org/10.1007/s11071-017-3401-9.

[11] Schmitendorf, W. E., and Barmish, B. R., "Null Controllability of Linear Systems with Constrained Controls," *SIAM Journal on Control and Optimization*, Vol. 18, No. 4, 1980, pp. 327–345. https://doi.org/10.1137/0318025, URL https://epubs.siam.org/doi/10.1137/0318025, publisher: Society for Industrial and Applied Mathematics.

[12] Kim, K., Rahili, S., Shi, X., Chung, S.-J., and Gharib, M., "Controllability and Design of Unmanned Multirotor Aircraft Robust to Rotor Failure," *AIAA Scitech 2019 Forum*, American Institute of Aeronautics and Astronautics, 2019. https://doi.org/0.2514/6.2019-1787, URL https://arc.aiaa.org/doi/abs/10.2514/6.2019-1787, _eprint: https://arc.aiaa.org/doi/pdf/10.2514/6.2019-1787.

[13] Tahavori, M., and Hasan, A., "Fault recoverability for nonlinear systems with application to fault tolerant control of UAVs," *Aerospace Science and Technology*, Vol. 107, 2020, p. 106282. https://doi.org/10.1016/j.ast.2020.106282, URL https://www.sciencedirect.com/science/article/pii/S1270963820309640.

[14] Stigter, J. D., van Willigenburg, L. G., and Molenaar, J., "An Efficient Method to Assess Local Controllability and Observability for Non-Linear Systems," *IFAC-PapersOnLine*, Vol. 51, No. 2, 2018, pp. 535–540. https://doi.org/10.1016/j.ifacol.2018.03.090, URL https://www.sciencedirect.com/science/article/pii/S2405896318300946.

[15] Lee, H., Kim, J., Kim, S.-h., Kim, M., and Kim, Y., "Local Strong Accessibility Analysis and Fault-Tolerant Control of Multicopter Considering Actuator Failures," *AIAA SCITECH 2023 Forum*, American Institute of Aeronautics and Astronautics, 2023, pp. AIAA 2023–2511. https://doi.org/10.2514/6.2023-2511, URL https://arc.aiaa.org/doi/abs/10.2514/6.2023-2511, _eprint: https://arc.aiaa.org/doi/pdf/10.2514/6.2023-2511.

[16] Johansen, T. A., and Fossen, T. I., "Control allocation—A survey," *Automatica*, Vol. 49, No. 5, 2013, pp. 1087–1103. https://doi.org/10.1016/j.automatica.2013.01.035, URL https://linkinghub.elsevier.com/retrieve/pii/S0005109813000368.

[17] Bodson, M., "Evaluation of Optimization Methods for Control Allocation," *Journal of Guidance, Control, and Dynamics*, Vol. 25, No. 4, 2002, pp. 703–711. https://doi.org/10.2514/2.4937, URL https://arc.aiaa.org/doi/10.2514/2.4937, publisher: American Institute of Aeronautics and Astronautics.

[18] Blanke, M., Christian Frei, W., Kraus, F., Ron Patton, J., and Staroswiecki, M., "What is Fault-Tolerant Control?" *IFAC Proceedings Volumes*, Vol. 33, No. 11, 2000, pp. 41–52. https://doi.org/10.1016/S1474-6670(17)37338-X, URL https://www.sciencedirect.com/science/article/pii/S147466701737338X.

[19] Zhang, Y., Rabbath, C. A., and Su, C.-Y., "Reconfigurable control allocation applied to an aircraft benchmark model," *2008 American Control Conference*, 2008, pp. 1052–1057. https://doi.org/10.1109/ACC.2008.4586631, iSSN: 2378-5861.

[20] Blanke, M., Kinnaert, M., Lunze, J., and Staroswiecki, M., "Fault Accommodation and Reconfiguration Methods," *Diagnosis and Fault-Tolerant Control*, Springer Berlin Heidelberg, Berlin, Heidelberg, 2016, pp. 389–466. https://doi.org/10.1007/978-3-662-47943-8_9, URL https://doi.org/10.1007/978-3-662-47943-8_9.

[21] Wu, N. E., Zhou, K., and Salomon, G., "Control reconfigurability of linear time-invariant systems," *Automatica*, Vol. 36, No. 11, 2000, pp. 1767–1771. https://doi.org/10.1016/S0005-1098(00)00080-7, URL https://www.sciencedirect.com/science/article/pii/S0005109800000807.

[22] Eisa, S. A., and Pokhrel, S., "Analyzing and Mimicking the Optimized Flight Physics of Soaring Birds: A Differential Geometric Control and Extremum Seeking System Approach with Real Time Implementation," *SIAM Journal on Applied Mathematics*, 2023, pp. S82–S104. https://doi.org/10.1137/22M1505566, URL https://epubs.siam.org/doi/abs/10.1137/22M1505566, publisher: Society for Industrial and Applied Mathematics.

[23] Morozov, Y. V., "Emergency Control of a Quadrocopter in Case of Failure of Two Symmetric Propellers," *Automation and Remote Control*, Vol. 79, No. 3, 2018, pp. 463–478. https://doi.org/10.1134/S0005117918030062, URL https://doi.org/10.1134/S0005117918030062.

[24] Lanzon, A., Freddi, A., and Longhi, S., "Flight Control of a Quadrotor Vehicle Subsequent to a Rotor Failure," *Journal of Guidance, Control, and Dynamics*, Vol. 37, No. 2, 2014, pp. 580–591. https://doi.org/10.2514/1.59869, URL https://arc.aiaa.org/doi/10.2514/1.59869, publisher: American Institute of Aeronautics and Astronautics.

[25] Mueller, M. W., and D'Andrea, R., "Stability and control of a quadrocopter despite the complete loss of one, two, or three propellers," *2014 IEEE International Conference on Robotics and Automation (ICRA)*, 2014, pp. 45–52. https://doi.org/10.1109/ICRA.2014.6906588, ISSN: 1050-4729.

[26] Lippiello, V., Ruggiero, F., and Serra, D., "Emergency landing for a quadrotor in case of a propeller failure: A backstepping approach," *2014 IEEE/RSJ International Conference on Intelligent Robots and Systems*, 2014, pp. 4782–4788. https://doi.org/10.1109/IROS.2014.6943242, ISSN: 2153-0866.

[27] Du, G.-X., Quan, Q., and Cai, K.-Y., "Controllability Analysis and Degraded Control for a Class of Hexacopters Subject to Rotor Failures," *Journal of Intelligent & Robotic Systems*, Vol. 78, No. 1, 2015, pp. 143–157. https://doi.org/10.1007/s10846-014-0103-0, URL https://doi.org/10.1007/s10846-014-0103-0.

[28] Brammer, R. F., "Controllability in Linear Autonomous Systems with Positive Controllers," *SIAM Journal on Control*, Vol. 10, No. 2, 1972, pp. 339–353. https://doi.org/10.1137/0310026, URL https://epubs.siam.org/doi/10.1137/0310026, publisher: Society for Industrial and Applied Mathematics.

[29] Nelson, R. C., *Flight stability and automatic control*, 2nd ed., WCB/McGraw Hill, Boston, Mass, 1998.

[30] Pratt, R., *Flight Control Systems: Practical Issues in Design and Implementation*, IET, 2000.

[31] Klein, G., Lindberg, R. E., and Longman, R. W., "Computation of a degree of controllability via system discretization," *Journal of Guidance, Control, and Dynamics*, Vol. 5, No. 6, 1982, pp. 583–588. https://doi.org/10.2514/3.19793, URL https://arc.aiaa.org/doi/10.2514/3.19793, publisher: American Institute of Aeronautics and Astronautics.

[32] Branch, M. A., Coleman, T. F., and Li, Y., "A Subspace, Interior, and Conjugate Gradient Method for Large-Scale Bound-Constrained Minimization Problems," *SIAM Journal on Scientific Computing*, Vol. 21, No. 1, 1999, pp. 1–23. https://doi.org/10.1137/S1064827595289108, URL https://epubs.siam.org/doi/10.1137/S1064827595289108, publisher: Society for Industrial and Applied Mathematics.

[33] Virtanen, P., Gommers, R., Oliphant, T. E., Haberland, M., Reddy, T., Cournapeau, D., Burovski, E., Peterson, P., Weckesser, W., Bright, J., van der Walt, S. J., Brett, M., Wilson, J., Millman, K. J., Mayorov, N., Nelson, A. R. J., Jones, E., Kern, R., Larson, E., Carey, C. J., Polat, İ., Feng, Y., Moore, E. W., VanderPlas, J., Laxalde, D., Perktold, J., Cimrman, R., Henriksen, I., Quintero, E. A., Harris, C. R., Archibald, A. M., Ribeiro, A. H., Pedregosa, F., van Mulbregt, P., and SciPy 1.0 Contributors, "SciPy 1.0: Fundamental Algorithms for Scientific Computing in Python," *Nature Methods*, Vol. 17, 2020, pp. 261–272. https://doi.org/10.1038/s41592-019-0686-2.

[34] Lambe, A. B., and Martins, J. R. R. A., "Extensions to the design structure matrix for the description of multidisciplinary design, analysis, and optimization processes," *Structural and Multidisciplinary Optimization*, Vol. 46, No. 2, 2012, pp. 273–284. https://doi.org/10.1007/s00158-012-0763-y, URL https://doi.org/10.1007/s00158-012-0763-y.

[35] "IEEE Guide for Information Technology - System Definition - Concept of Operations (ConOps) Document," *IEEE Std 1362-1998*, 1998, pp. 1–24. https://doi.org/10.1109/IEEESTD.1998.89424.

[36] Delbecq, S., Budinger, M., Ochotorena, A., Reysset, A., and Defay, F., "Efficient sizing and optimization of multirotor drones based on scaling laws and similarity models," *Aerospace Science and Technology*, Vol. 102, 2020, p. 105873. https://doi.org/10.1016/j.ast.2020.105873, URL https://linkinghub.elsevier.com/retrieve/pii/S1270963820305551.

[37] Pollet, F., Delbecq, S., Budinger, M., and Moschetta, J.-M., "Design optimization of multirotor drones in forward flight," *32nd Congress of the International Council of the Aeronautical Sciences*, 2021.

[38] Pollet, F., Delbecq, S., Budinger, M., Moschetta, J.-M., and Liscouet, J., "A common framework for the design optimization of fixed-wing, multicopter and VTOL UAV configurations," *33rd Congress of the International Council of the Aeronautical Sciences*, 2022.

[39] E-flite, "Ultra Stick 25e," , 2022. URL https://www.e-fliterc.com/product/ultra-stick-25e-arf-50/EFL4025.html.

[40] Dorobantu, A., Murch, A., Mettler, B., and Balas, G., "System Identification for Small, Low-Cost, Fixed-Wing Unmanned Aircraft," *Journal of Aircraft*, Vol. 50, No. 4, 2013, pp. 1117–1130. https://doi.org/10.2514/1.C032065, URL https://arc.aiaa.org/doi/10.2514/1.C032065, publisher: American Institute of Aeronautics and Astronautics.

[41] Leng, Y., Moschetta, J.-M., Jardin, T., and Bronz, M., "An analytical model for propeller aerodynamic efforts at high incidence," *54th 3AF International Conference on Applied Aerodynamics*, Paris, FR, 2019. URL https://oatao.univ-toulouse.fr/28445/.